Seismic velocity structure of the Tonga-Kermadec - Louisville Ridge collision zone

1 **Seismic velocity structure and deformation due to the collision of the**

2 **Louisville Ridge with the Tonga-Kermadec Trench**

3

4 W. Stratford[1*], C. Peirce[1], M. Paulatto[2], M. Funnell[1], A.B. Watts[2], I. Grevemeyer[3] and D.

5 Bassett[2]

6 *[1]Department of Earth Sciences, Durham University, Durham, DH1 3LE, United Kingdom*

7 *(w.r.stratford@durham.ac.uk)*

8 *[2]Department of Earth Sciences, Oxford University, Oxford, OX1 3AN, United Kingdom*

9 *[3]GEOMAR, Helmholtz Centre of Ocean Research, 24148 Kiel, Germany*

10 ** Now at GNS Science, Lower Hutt, 5011, New Zealand*

11 Accepted date. Received date; in original form date

12

13 Abbreviated title: Seismic velocity structure of the Tonga-Kermadec - Louisville Ridge
14 collision zone

15 Corresponding Author:
16 Wanda Stratford
17 Department of Earth Sciences
18 Durham University
19 DH1 3LE
20 Durham
21 United Kingdom
22 Ph: +44 (0) 191 33 42357
23 Email: wandastratford@gmail.com

24

25

1
2
3
4 25   **Seismic velocity structure and deformation due to the collision of the**
5
6 26   **Louisville Ridge with the Tonga-Kermadec Trench**
7
8 27
9
10 28   W. Stratford[1], C. Peirce[1], M. Paulatto[2], M. Funnell[1], A.B. Watts[2], I. Grevemeyer[3] and D.
11 29   Bassett[2]
12
13 30   *[1]Department of Earth Sciences, Durham University, Durham, DH1 3LE, United Kingdom (w.r.stratford@durham.ac.uk)*
14 31   *[2]Department of Earth Sciences, Oxford University, Oxford, OX1 3AN, United Kingdom*
15 32   *[3]GEOMAR, Helmholtz Centre of Ocean Research, 24148 Kiel, Germany*
16 33   ** Now at GNS Science, Lower Hutt, 5011, New Zealand*
17 34
18 35
19
20 36   **SUMMARY**
21
22 37   New marine geophysical data recorded across the Tonga-Kermadec subduction zone are used to
23 38   image deformation and seismic velocity structures of the forearc and Pacific plate where the
24 39   Louisville Ridge seamount chain subducts. Due to the obliquity of the Louisville Ridge to the trench
25 40   and the fast 128 mm yr^{-1} south-southwest migration of the ridge-trench collision zone, post-, current
26 41   and pre-seamount subduction deformation can be investigated between 23° and 28°S. We combine
27 42   our interpretations from the collision zone with previous results from the post-and pre collision zones
28 43   to define the along-arc variation in deformation due to seamount subduction. In the pre-collision zone
29 44   the lower-trench slope is steep, the mid-trench slope has ~3 km thick stratified sediments and
30 45   gravitational collapse of the trench slope is associated with basal erosion by subducting horst and
31 46   graben structures on the Pacific plate. This collapse indicates that tectonic erosion is a normal process
32 47   affecting this generally sediment starved subduction system. In the collision zone the trench-slope
33 48   decreases compared to the north and south, and rotation of the forearc is manifest as a steep plate
34 49   boundary fault and arcward dipping sediment in a 12-km-wide, ~2-km-deep mid-slope basin. A ~3
35 50   km step increase in depth of the middle and lower crustal isovelocity contours below the basin
36 51   indicates the extent of crustal deformation on the trench slope. At the leading edge of the overriding
37 52   plate, upper crustal P-wave velocities are ~4.0 km s^{-1} and indicate the trench fill material is of
38 53   seamount origin. Osbourn Seamount on the outer rise has extensional faulting on its western slope and
39 54   mass wasting of the seamount provides the low V_p material to the trench. In the post-collision zone to
40 55   the north, the trench slope is smooth, the trench is deep, and the crystalline crust thins at the leading
41 56   edge of the overriding plate where V_p is low, ~5.5 km s^{-1}. These characteristics are attributed to a
42 57   greater degree of extensional collapse of the forearc in the wake of seamount subduction. The
43 58   northern end of a seismic gap lies at the transition from the smooth lower-trench slope of the post-
44 59   collision zone, to the block faulted and elevated lower-trench slope in the collision zone, suggesting a
45 60   causative link between the collapse of the forearc and seismogenesis. Along the forearc, the transient
46 61   effects of a north-to-south progression of ridge subduction are preserved in the geomorphology,

Seismic velocity structure of the Tonga-Kermadec - Louisville Ridge collision zone

62 whereas longer-term effects may be recorded in the ~80 km offset in trench strike at the collision zone

63 itself.

64

65 **Key words:** Subduction zone processes, volcanic arc processes, crustal structure, controlled source

66 seismology

67

68 1   INTRODUCTION

69 High convergence rates and a rapid south-southwest migrating collision zone (Lonsdale, 1986;

70 MacLeod, 1994) make the Tonga-Kermadec Trench–Louisville Ridge collision zone an ideal location

71 to study the effect of seamount subduction on lithospheric structure. Here a major change in tectonic

72 regime in the backarc, a lateral offset in the trench (Ruellan *et al.*, 2003), and a zone of elevated and

73 deformed forearc coincide with the subduction of the Louisville Ridge (Bonnardot *et al.*, 2007). The

74 seamounts of the ridge exceed 3.5 km in relief above the seafloor and are carried into the subduction

75 zone at ~70 mm yr^{-1}, one of the highest global rates of subduction (DeMets *et al.*, 1994).

76 Deformation of the forearc and trench, during and in the wake of subduction of buoyant

77 features, is observed at subduction zones globally (Stern, 2011). The two main tectonic erosion

78 processes in a subduction zone are frontal erosion of the overriding plate, and basal erosion, whereby

79 structures on the subducting plate or high pressure fluids released during subduction erode the forearc

80 crust from beneath (Clift & Vannucchi, 2004; Stern, 2011).   Rapid rotation and uplift followed by

81 subsidence of the forearc are attributed to subduction of topographic edifices at a number of

82 subduction systems – e.g. New Hebrides and Solomon (Taylor *et al.*, 2005), Banda Arc (Fleury *et al.*,

83 2009), Costa Rica (Sak *et al.*, 2009), Peru (Clift & Pecher, 2003) and Cascadia (Trehu *et al.*, 2012).

84 These deformation processes may be transient but are recorded in uplifted marine terraces and as

85 differential offsets of forearc blocks on faults at high angles to the trench (Fisher *et al.*, 1998). In

86 addition, thickening of the forearc crust by tectonic underplating of subducted forearc material may

87 also occur (Stern, 2011; Geist *et al.*, 1993).

88 Once the seamount passes beneath the plate boundary interface, the forearc subsides and

89 undergoes gravitational collapse (Taylor *et al.*, 2005; Laursen *et al.*, 2002; Wright *et al.*, 2000;

90 Ballance *et al.*, 1989), with forearc erosion occurring until the pre-seamount subduction forearc taper

91 is re-established (Lallemand *et al.*, 1992). Evidence of seamount subduction may be recorded by the

92 rotation of sediment layers in the forearc (Clift *et al.*, 1998), as irregularities or indentations in the

93 trench in the wake of seamount subduction (Trehu *et al.*, 2012), or as an overall offset in the plate

94 boundary (Ruellan *et al.*, 2003; Wright *et al.*, 2000; Lallemand *et al.*, 1992).

95 Erosion of the deformed forearc in the wake of seamount subduction is inferred to have caused

96 a ~80 km offset in the trench north of the current Tonga-Kermadec Trench–Louisville Ridge collision

97 zone (Lallemand *et al.*, 1992; Wright *et al.*, 2000; von Huene & Scholl, 1991). However, the plate

Seismic velocity structure of the Tonga-Kermadec - Louisville Ridge collision zone

98   boundary as a whole is considered to be an erosive margin (Clift & Vannucchi, 2004; Clift &

99   MacLeod, 1999). As subduction of the Pacific plate at the Tonga-Kermadec Trench is fast (DeMets *et*

100   *al.*, 1994) and sediment poor (Heuret *et al.*, 2012), tectonic erosion of the overlying plate is inferred to

101   be a general process affecting this plate boundary (Clift & MacLeod, 1999). Horst and graben

102   structures formed by bending-induced extension at the outer rise can enhance frontal and basal

103   erosion of the overlying plate, particularly when the trench is sediment starved (Stern, 2011; von

104   Huene & Scholl, 1991).

105   To distinguish seamount subduction-related deformation from normal Tonga-Kermadec erosive

106   subduction, the "before, during and after" regions have been the target of a number of marine

107   geophysical surveys in recent years (Herzer & Exon, 1985; Crawford *et al.*, 2003; Contreras-Reyes *et*

108   *al.*, 2011; Clift *et al.*, 1998; Ballance *et al.*, 1989); the most recent being the R/V Sonne cruise SO215

109   in 2011 (Peirce & Watts, 2011). Previous studies have investigated the effect of seamount subduction

110   on the geomorphology of the Tonga-Kermadec subduction zone and have focused on the along-arc

111   changes in seafloor features in the forearc and trench (Wright *et al.*, 2000; Clift *et al.*, 1998).

112   However, the effects of seamount subduction extend far beneath the surface and studies of the crust

113   and upper mantle are required to fully understand the short-to-long-term effect seamount subduction

114   has on the overriding plate. Here, we describe seismic and density models of the crust and upper

115   mantle in the current seamount collision zone, and compare them to previous seismic studies in the

116   post-collision zone to the north (Contreras-Reyes et al., 2011) and the pre-collision zone to the south

117   (Funnell *et al*., 2014) to interpret the along arc variation in deformation associated with the

118   subduction of the Louisville Ridge seamount chain.

119

2   GEOLOGICAL SETTING

121   Subduction of the Pacific plate beneath the Indo-Australian plate began in the Eocene at the Tonga-

122   Kermadec Trench (Sutherland, 1999; Malahoff *et al*., 1982). Plate convergence rates vary from 80

123   mm yr^{-1} at 17°S to 45 mm yr^{-1} at 39°S (DeMets *et al*., 1994). This seemingly linear, 2000-km-long

124   subduction system is subdivided at its intersection with the Louisville Ridge at 26°S (Fig. 1) into the

125   Tonga Ridge to the north and the Kermadec Ridge to the south. These ridges were formed by arc

126   magmatism during the initial building of the forearc in the Eocene (Bloomer *et al*., 1994; Tappin,

127   1994).

128   The Tonga Ridge is broad, elevated, flat-topped, and capped with sediment and has undergone

129   several extensional collapse events since opening of the Lau Basin began in the late Miocene (Herzer

130   & Exon, 1985). In contrast, to the south the Kermadec Ridge is narrow with a forearc basin that

131   contains strata dipping towards the trench. The differences between the ridges have been attributed to

132   either along-arc variation in Miocene post-rifting structure (Parson & Hawkins, 1994), or the Tonga

133   Ridge being altered by Louisville Ridge subduction (Pelletier & Dupont, 1990; Dupont & Herzer,

134   1985). A decrease in the arc-trench gap beneath the Kermadec Ridge, compared to the Tonga Ridge to

135   the north, may be indicative of an increase in slab dip south of the collision zone (Bonnardot *et al.*,

136   2007).

137   Predominately of basaltic composition, the ~4000-km-long Louisville Ridge seamount chain

138   intersects the Tonga-Kermadec Trench at an angle of ~36°. The ridge is not strictly linear, its track

139   undulates and can be divided into ~200-km-long segments offset by small changes in strike (Fig. 1,

140   inset). The ridge was formed by the passage of the Pacific plate over the Louisville Hotspot, which is

141   presently located near the intersection of the Eltanin Fracture Zone with the East Pacific Rise

142   (Lonsdale, 1986; Watts *et al.*, 1988). Temporal variations in magmatic productivity of the hotspot

143   have been inferred with a general waning with time (Koppers *et al.*, 2004; Watts *et al.*, 1988). The

144   ridge has been dated from dredge samples and analysis of IODP drilling samples (e.g. Koppers *et al*,

145   (2004); Koppers *et al*, (2012); Expedition 330 Scientists, (2012) and its obliquity to the trench is

146   inferred to have been greater in the past, with a decreasing southward progression of ridge subduction

147   rate with time from 283 mm yr^{-1} at 3.5 Ma to the current rate of 128 mm yr^{-1} (Ruellan *et al.*, 2003).

148   In the Lau Basin to the north of the ridge-trench collision zone, backarc spreading occurs in a

149   wedge-shaped area (Weissel, 1979; Ruellan *et al.*, 1994). To the south, extension occurs in the Havre

150   Trough, convergence rates are slower and the backarc is more rectangular in shape (Fig. 1, inset).

151   This significant change in the style of backarc extension is attributed to the effects of subduction of

152   seamounts on the locking/unlocking of the subduction system (Ruellan *et al.*, 2003).

153   Changes in forearc properties are manifest in a ~150-km-wide zone of deformation at the ridge-

154   trench collision. In addition, the zone is associated with a region of reduced seismic activity compared

155   to the north and south, especially in shallow and intermediate depth seismicity. Seismic gaps are

156   associated with the fracturing and interplate weakening effects of subducting relief (Wang & Bilek,

157   2014). However, the seismic gap at the Louisville Ridge is wider than the seamount edifices being

158   subducted and is broadly similar in size to the footprint of the flexural moats flanking the subducting

159   ridge and to the forearc collision zone. The association of the seismic gap with the ridge suggests that

160   the stress state of the overriding plate has been altered by the subducting seamounts and their flexural

161   moats (Bonnardot *et al.*, 2007). Three large earthquakes (M_w=7.4-7.5) located in close proximity to

162   the subducting Louisville Ridge have been attributed to near-surface locking effects (Christensen &

163   Lay, 1988).

164   Multichannel seismic reflection data acquired across the collision zone in the late 1980s image

165   an arcward-dipping reflector beneath the lower-trench slope at ~25.5°S (Ballance *et al.*, 1989).

166   Ballance *et al*. (1989) associate this reflector with the top surface of a subducted seamount, naming it

167   Motuku (Fig. 1). The inferred seamount is on the same strike as the three oldest Louisville Ridge

168   seamounts and at a similar along-ridge spacing, lying half way between Profile A of SO215 (Peirce &

169   Watts, 2011) and Profile P02 (Fig. 1) of an earlier R/V Sonne cruise SO195a ((Contreras-Reyes *et al.*,

170   2011).

171   The ~78 Ma Osbourn Seamount (Clouard & Bonneville, 2005; Koppers *et al.*, 2012) is

172   currently riding the outer rise seaward (east) of the Tonga-Kermadec Trench and will be the next in

173   the chain to be subducted. The trench floor directly arcward of Osbourn Seamount shallows by 3000

174   m, compared to just north and south of the collision zone, and comprises a broad zone of faulted

175   blocks. The adjacent forearc is also elevated by ~300 m compared to the forearc to the north. Seabed

176   imaging here reveals a zone of extensive faulting with large-scale mass wasting events forming

177   canyons and sediment pathways across the outer forearc, indicating a region of instability and

178   progressive uplift (Clift *et al.*, 1998).

179

180   **3   MARINE GEOPHYSICAL DATA**

181   Over 1500-line kilometres of geophysical data were acquired during R/V Sonne cruise SO215 (Peirce

182   & Watts, 2011). Swath bathymetry, gravity, magnetics, parasound and multichannel seismic (MCS)

183   and wide-angle seismic data were acquired contemporaneously along five profiles. Profile A,

184   presented in this paper (Fig. 1) is a coincident wide-angle and MCS profile that intersects the trench at

185   a high angle, crossing the forearc, trench and Osbourn Seamount at the Louisville Ridge collision

186   zone. All models and seismic profiles presented here are aligned by a common co-ordinate reference

187   system in which 0 km is located at the trench axis and positive model and profile offsets are towards

188   the east.

189

190   **3.1 MCS data**

191   The primary purpose of the MCS data acquisition was to image layer thicknesses and internal

192   structure in the sedimentary succession along the wide-angle profile to provide constraint to the

193   shallow section of the ray-trace model. Twelve Sercel G-guns in two, six-gun sub-arrays and

194   comprising a total volume of 5440 in^3, were used as the seismic source. This array was carefully

195   tuned for contemporaneous MCS and wide-angle acquisition, and to address the energy scattering and

196   propagation challenges of a thin pelagic sediment cover (Heuret *et al.*, 2012; Menard *et al.*, 1987;

197   Zhou & Kyte, 1992; Burns *et al*., 1973; Lonsdale, 1986) and the large and rapid lateral variation in

198   seafloor morphology and relief (Fig. 1). Shots were fired at 60 s intervals (~150 m shot spacing at a

199   surveying speed of 4.5 kn) to minimise water-wave wrap-around in the wide-angle data. These shots

200   were recorded using a 3-km-long, 240-channel streamer with a 12.5 m group interval and towed at

201   ~10 m depth, and resulted in a data fold of ~10.

202   A simple pre-stack processing sequence was applied including common depth point (CDP)

203   sorting into 25 m bins, normal move-out correction and surface consistent deconvolution. A

204   Butterworth filter (band-pass range: 3-10-100-120 Hz) was used to remove high amplitude sea swell

205   and wave noise. Velocity analysis included velocity picking at a spacing of 10-100 CDPs horizontally

206 (depending on the rate of lateral variability) and 0.1-0.3 s two-way travel-time (TWTT) vertically.

207 Below basement a simple velocity gradient was assumed and extrapolated to the bottom of the record

208 section as no distinct intra-crustal primary reflections are observed. To minimize the amplitude of the

209 seafloor multiple, a post-stack deconvolution filter was designed using the primary reflection from a

210 region of smooth, flat-lying seafloor. Post-stack, constant velocity (1.5 km s^{-1}) Kirchhoff migration

211 was applied to reduce the appearance of seabed-scatter diffraction tails. For final section plotting (Fig.

212 2), a water column mute, mean trace scaling and automatic gain compensation were applied.

213

214 **3.2 Wide-angle seismic data**

215 Thirty ocean-bottom seismographs (OBSs), each with a hydrophone and a three-component geophone

216 package as sensors, were deployed along Profile A at ~12 km spacing and in water depths of up to

217 6000 m. Four expendable bathymetric thermographs spread evenly along the profile were deployed

218 contemporaneously with the OBSs and used to determine the water column velocity structure. The

219 resulting velocity-depth profiles were referenced back to a sound velocity profile to 3000 m depth

220 conducted at the start of the cruise to calibrate the swath bathymetry data. As part of record section

221 creation, OBSs were relocated to their correct seafloor position by modelling the arrival times of the

222 water wave and seafloor-sea surface multiple. The final record sections (e.g. Figs 3a, 4a and 5a) can

223 be divided, on the basis of their signal-to-noise ratio (SNR), into three main tectonic regimes - the

224 Tonga Ridge, the trench and the subducting Pacific plate - and the general characteristics of the data

225 from each of these three regions are discussed below.

226

227 *3.2.1 Tonga Ridge*

228 OBSs deployed across the Tonga Ridge recorded arrivals to ~100 km shot-receiver offset (Fig. 3a).

229 Sediment arrivals from the forearc (P_s) are observed for ~8 km shot-receiver offset in the west (Fig.

230 3a), decreasing to 5 km in the east, and crustal diving waves (P_g) are observed from ~5 to 70 km shot-

231 receiver offset (Figs 3b and c). Refracted arrivals from the upper mantle (P_n) are observed at longer

232 offsets (>70 km). Moho reflections (P_mP) are only recorded by OBS A20, most likely due to better

233 coupling at this locality as P_g and P_n arrivals are also observed to greater offsets than elsewhere on the

234 forearc.

235

236 *3.2.2 Trench*

237 Signal attenuation decreases westward (Fig. 4a) with crustal arrivals observed only over shot-receiver

238 offsets <30 km on OBSs located on the outer trench wall, but increasing to >70 km by the inner-

239 trench wall. In the trench, near-offset arrivals are observed but are labelled P_g and not P_s, as distinct

240 sedimentary layers are only observed on the coincident MCS record section at the mid-trench slope

241 (Fig. 2a, offset -75 km). P_n arrivals are observed over shot-receiver offsets of 60-120 km.

242

Seismic velocity structure of the Tonga-Kermadec - Louisville Ridge collision zone

243   *3.2.3 Pacific plate*

244   On OBSs located on the flanks of Osbourn Seamount (OBSs A9-A12 – Fig. 1), seamount topography

245   produces significant variation in P_g arrival times. P_g arrivals that have propagated through the edifice

246   are observed to ~4 km shot-receiver offset for OBSs located on the eastern flank, increasing to ~8 km

247   offset at its centre. Arrivals from the middle crust are observed from ~ 4-8 km to 40 km offset and an

248   intra-crustal reflection (P_iP) is observed on the eastern side of the seamount (Figs 5c and d). P_n

249   arrivals from beneath the seamount are recorded on the eastern flank OBSs (A4-A9), and in the trench

250   (OBSs A14 and A12). Arrivals from the Moho are observed on the mid-trench slope OBSs (A16-

251   A19) and are recorded in the shot-receiver offset range of 30-40 km for P_mP and 80-120 km for P_n.

252   Most OBSs located on the Pacific plate recorded P_mP and P_n arrivals at 30-40 km and >40 km offsets,

253   respectively.

254

255   **3.3 Wide-angle forward modelling**

256   Using stacking velocities, sediment thicknesses and intra-sediment interface depths were calculated

257   from the MCS data and used to build the upper part of the initial starting model for wide-angle ray-

258   trace modelling. The water column was added using the depth to seabed, and a velocity structure

259   derived from the expendable bathymetric thermographs deployed along the profile.

260   Forward modelling of P-wave arrival times was undertaken using *rayinvr* (Zelt & Smith, 1992).

261   In general, first arrival travel-times were picked from OBS record sections with a 2 Hz high-pass filter

262   applied to remove low-frequency sea swell and wave noise. In regions where low SNR levels

263   hampered arrival picking, a broad band-pass filter (2-4-12-25 Hz) was applied, and these travel-time

264   picks were down-weighted and modelled with larger uncertainties (150 ms). Pick uncertainties were

265   assigned on the basis of SNR, and resulted in location and offset dependent values (see Table 1).

266   Initially only travel-times picked from high-pass filtered data were included in order to achieve the

267   first-pass fit, before adding those derived from band-pass filtered data (Figs 3-5).

268   Modelling followed a top-down approach, fitting first the sediment and upper crustal arrivals

269   prior to tracing progressively deeper layers and fitting the longer offset, lower crust and uppermost

270   mantle arrivals. For each layer, the arrivals from a subset of adjacent instruments were modelled

271   simultaneously and a 'rolling window' approach was adopted to extend the fit along the length of the

272   profile.

273   The fit of calculated arrivals to the travel-time picks (Figs 3-5) was initially qualitatively

274   assessed to produce a model that approximately satisfied the observed data. Subsequently, analysis of

275   RMS travel-time misfit and the χ^2 parameter (Zelt & Smith 1992) provided a quantitative assessment

276   and acted as a statistical indicator when making minor adjustments to further refine model fit. A χ^2 of

277   1 is considered a good fit, while a χ^2 of <1 is regarded as an over-fit to the observed travel-time picks.

278   In this study a χ^2 of <2.6 is considered an acceptable fit.

279

Seismic velocity structure of the Tonga-Kermadec - Louisville Ridge collision zone

3.4 Best-fit model testing

A fit within a χ^2 of <2.6 does not guarantee the uniqueness of the model as an arrival travel-time is dependent not only on seismic velocity but also propagation path length. Consequently, an acceptable fit can be obtained by trade-off of one of these parameters against the other. To estimate the model uncertainties associated with this trade-off, the resolution and uniqueness of the final, best-fit velocity-depth model were tested by: a) sensitivity testing; b) fit to MCS reflectivity; and c) gravity modelling.

3.4.1 Sensitivity testing

The final, best-fit model was sensitivity tested to determine the resolution in depth and geometry of the individual layer boundaries (ΔZ) and the resolution of layer velocities (ΔV_p), whilst still achieving an acceptable fit to within the errors (Table 2). A model was considered an acceptable fit while the RMS errors remained within double the pick uncertainty (Table 1) of the layer being tested (Table 2). This approach shows final model velocities are constrained to within ± 0.10 km s^{-1} from the seabed to the Moho, except for the outer forearc region where the velocity at the Moho is constrained only to ± 0.15 km s^{-1}. Similarly, by varying the depth to and thickness of each layer systematically, testing showed that these parameters are constrained to better than ± 1.0 km throughout the model except in the outer forearc region where Moho depth is only resolved to ± 2.0 km.

3.4.2 Fit to MCS reflectivity

To compare the final, best-fit wide-angle model (Fig. 6b) with the MCS data (Fig 2b), Profile A was reprocessed using a stacking velocity model created by combining the crustal wide-angle velocity model with the velocity picks made from the sediment layers observed in the original MCS data section. Having first resorted and reapplied the geometry for a finer CDP bin interval of 12.5 m, a pre-stack time-migration process was applied and the data re-stacked. This approach provides a means of testing the non-uniqueness of the forward model, since interface depths and geometries interpreted independently from analysis of both data types should match within the uncertainties of each method. The depths to the interfaces of the final wide-angle model were converted to TWTT and overlain on top of MCS Profile A (e.g. Figs 2b, 5d and 7). Although the lateral resolution of the wide-angle model is lower than that of the MCS data, the TWTT converted interfaces agree within the depth uncertainties (± 0.5 km for sedimentary interfaces and crustal reflectors of the Pacific plate and ± 1 km for the Moho) derived from the sensitivity testing.

3.4.3 Gravity modelling

Gravity modelling was used as the final stage of uniqueness testing. This modelling also provided additional constraint on the two areas of the model with sparse ray coverage: i) the lower crust and Moho of the outer 60 km of the forearc; and ii) the location and dip of the subducted slab beneath the

317   overriding plate (Fig. 6b). The recorded shipboard free-air gravity anomaly (Fig. 6c) was modelled

318   using *grav2d*, a 2-D modelling code based on the polygon approach of Talwani *et al*. (1959). Leaving

319   interface depths unchanged, the velocities from the best-fit wide-angle model were used to define the

320   framework of the density-depth model. Laterally dividing the layers into additional polygons

321   accommodated significant changes in V_p within a model layer (Fig. 6d). The mean V_p in each polygon

322   was then used to calculate its bulk density using standard velocity-density relationships (Ludwig *et al*.,

323   1970; Brocher, 2005).

324   The gravity anomaly over the Pacific plate and trench, including the shallow slab position, are

325   fitted with the seismically constrained density model. However, a long wavelength positive signal

326   extends across the forearc and is attributed the subducted Pacific plate lithosphere beneath the forearc

327   (Fig. 6c and d). To model this long wavelength anomaly, the position and dip of the slab from 25 to

328   300 km depth within the model was defined using other Wadati-Benioff zone seismogenesis studies,

329   coupled with a compilation of slab structures derived from active- and passive-source seismological

330   studies (Hayes *et al*., 2012; Bonnardot *et al*., 2007). Below 100 km the lithospheric mantle of the slab

331   was modelled with a density contrast of 40 kg m^{-3} with the surrounding mantle. This density contrast

332   is a mid-range value for the Pacific plate at depth at the Tonga-Kermadec subduction system (Billen

333   *et al*., 2003), and used elsewhere to model the subducting Pacific plate (e.g. Aleutian arc: Watts &

334   Talwani, (1974). Densities in the section of the Pacific plate crust subducted beneath the forearc were

335   also increased by ~150 kg m^{-3}, in keeping with studies that show a density increase resulting from

336   dewatering and phase changes with increasing pressure and temperature (e.g. Hacker *et al*., 2003).

337   A good fit to the observed free-air anomaly was achieved without adjusting the seismically

338   well-constrained part of the model, only by assigning the forearc mantle, between 100 and 300 km

339   depth, a density contrast of -20 kg m^{-3} over a ~500-km-wide region (-30 kg m^{-3} between 25 and 100

340   km depth). This is consistent with previous geodynamic models of the Tonga subduction zone which

341   also require a broad region of low density in the mantle wedge (-20 kg m^{-3}), extending hundreds of

342   kilometres west of the trench, to model the seafloor topography (Billen *et al.*, 2003).

343

344   **4. INTERPRETATION OF PROFILE A.**

345   We describe the final, best-fit wide-angle model for the collision zone (Profile A - Fig. 6b) by tectonic

346   section, west-to-east, from the Tonga Platform to the Pacific plate. In addition, lateral variations in

347   velocity layer and crustal thicknesses, and average velocities, between the arc and the trench are

348   highlighted with a series of one-dimensional velocity-depth profiles, spaced at 25-50 km intervals

349   (Fig. 8).

350

351   **4.1 Tonga Platform**

352   An up to 1500 m thick sequence of Oligocene-Recent volcaniclastics, pelagic chalks and carbonates

353   with velocities of 2.0-2.5 km s^{-1} is deposited on the Tonga Ridge. These sediments undulate in

354 thickness above a basement surface that is offset on steep normal faults (Fig. 6b). Extensional

355 collapse towards the backarc is observed in tilting of sediment layers in the west (Fig. 6b, -200 to -170

356 km). Beneath the outer-arc high the basement is extended by small-scale distributed faulting (Fig. 6b,

357 offsets -115 to -95 km) which most likely post-dates the deformation on the rest of the ridge (Fig. 6b,

358 -170 to -115 km), as the resulting accommodation space is not yet sediment filled. The forearc

359 crystalline crust comprises an Eocene basement where P-wave velocities are 3.5-4.5 km s^{-1}, increasing

360 to 4.0-5.0 km s^{-1} beneath the outer-arc high (Fig. 6a). Basement velocities are slow on the western

361 side of the ridge, where V_p of ~5.5 km s^{-1} extends to ~7 km depth. Average velocity in the middle and

362 lower crust decreases by 0.3 km s^{-1} from east-to-west (Fig. 8), indicating a change in crustal structure

363 across the ridge. The Moho depth is constrained by reversed P_n arrivals (Vp ~7.8 km s^{-1}) from the

364 mid-trench slope arcward and is 18±1 km.

365

366 **4.2 Trench slope**

367 Sediment is transported eastward from the Tonga Ridge to a ~12-km-wide mid-slope basin via a

368 broad and shallow, ~50-km-wide, series of trench-perpendicular canyons (Figs 9c and d, offset -80

369 km). The basin is the only region in the trench where a significant accumulation of sediment is

370 identified on the MCS data (Fig 2b, offset -75 km) and has two distinct units: i) an upper ~2-km-thick

371 unit with distinct depositional layers and ii) a lower, diffusely reflective unit. These two units most

372 likely represent different phases of extension. The mid-slope basin is located above a sharp, ~3 km

373 increase in the depth to the >6.0 km s^{-1} middle and >6.5 km s^{-1} lower crust. These lateral changes in

374 velocity structure demonstrate the full crustal scale of the present extensional deformation of the

375 forearc.

376   The ~60-km-wide lower-trench slope has a shallow angle and rapid lateral variation in seafloor

377 relief (Fig. 9c). A ~2 km topographic high in the centre of the slope (Fig. 6a, offset -35 km) is flanked

378 to the east, north and south by basins and to the northeast and southwest by ramparts, where relatively

379 low velocities (3.5-4.0 km s^{-1}) extend to ~5 km beneath the seafloor. The high has a velocity of 4.0

380 km s^{-1} at the seafloor increasing to 5.5 km s^{-1} by 6 km depth (Fig. 9d). While of higher velocity in the

381 near surface compared to the east and west, in the middle crust the <6 km s^{-1} velocity zone extends to

382 a greater depth beneath the edifice than its surrounds.

383

384 **4.3 Trench axis and the plate boundary**

385 The trench floor on Profile A is ~3 km shallower than to the north and south, and is congested with

386 material carried into the trench on the subducting plate and by material of forearc provenance. The

387 subducting, ~10 km wide, Mo'unga Seamount (Ballance *et al.*, 1989; Pointoise *et al.*, 1986) creates a

388 disparity between the geomorphic and tectonic trench axis locations and broadens the trench floor

389 (Figs 6b, 9c and d). The geomorphic trench, the deepest part of the collision zone, is east of the

390 seamount at the base of a graben that forms part of a region of extensional faulting on the seaward

391   wall of the subducting Pacific plate (Fig. 9c). The true plate boundary lies on the arcward side of the

392   seamount, where a fault separates the forearc from trench fill originating from the Pacific plate (Fig.

393   6b, inset), and can be traced ~20 km to the west. Small-scale thrust faulting intersects the seafloor

394   (Fig. 6b inset, offset -10 km) 10 km west of the fault on the arcward side of the ramparts of low-

395   velocity material.

396   At the plate boundary, the forearc crustal thickness is estimated to be ~12 km (including

397   sediment and low V_p deformed forearc rock) where it abuts the subducting Pacific plate, and the

398   down-dip plate interface width is ~26 km (Fig. 8d). Although poorly constrained, decreasing upper

399   mantle velocities in the mantle wedge below this part of the outer forearc to 7.5 km s^{-1}, where P_mP and

400   P_n arrivals cross between the subducting and overriding plates (Figs 5a and b, offsets -30 to -60 km),

401   improves the model fit to the long travel-path arrival times.

402

403   **4.2 Osbourn Seamount**

404   Outer-rise bend faults on the subducting Pacific plate trend sub-parallel to the trench strike on the

405   north side of Osbourn Seamount becoming more parallel to the south (Fig. 9c). The vertical relief

406   across these faults is ~200 m and they cut through the western flank of the seamount and down-step it

407   into the trench. The outer trench wall is pervasively faulted with a 3 to 4-km-thick layer of velocity

408   3.5-4.5 km s^{-1} extending to ~4 km beneath seafloor (Fig. 9d). These velocities suggest that material

409   entering the trench here is not composed of low-velocity pelagic sediment, but is predominantly of

410   seamount origin and most likely comprises lavas, volcanic breccia and volcaniclastic sediments. This

411   material is inferred to be highly fractured and fluid saturated, both of which may contribute to the low

412   velocities observed (Moos & Zoback, 1983).

413   The summit of Osbourn Seamount has a ~200 m thick veneer of sediment with velocities of ~2

414   km s^{-1}. On the eastern side of the edifice (Fig. 5a, offsets 60-120 km) the sediment layer thickens and

415   velocities increase to 3.0 km s^{-1} at its base. Due to the low accumulation rates of pelagic material

416   (Heuret *et al.*, 2012; Menard *et al.*, 1987; Zhou & Kyte, 1992; Burns *et al.*, 1973; Lonsdale, 1986),

417   and its semi-stratified nature, this layer is most likely predominantly composed of primary and

418   reworked (mass wasting) volcaniclastic products from the seamount. Velocities within the seamount

419   edifice are 4.5-5.5 km s^{-1}, which are representative of volcanic rock of basaltic composition

420   (Christensen & Mooney, 1995). In the middle crust velocities are 6.4-6.5 km s^{-1} (Fig. 6a, offsets 20 –

421   60 km), compared to >6.6 km s^{-1} of the oceanic crust to the east. The middle crust beneath the

422   seamount shoals, tilts arcward, thickens, and has an apparent offset to the west. Similarly, a ~30-km-

423   wide region of high V_p (~7.1 km s^{-1}) lower crust also has an apparent offset to the west. This offset

424   may be due to the strike of the seismic profile being to the north of the seamount summit and/or the

425   tilting and mass wasting of the low V_p volcaniclastics that cover the seamount as it enters the trench.

426   Beneath the seamount a crustal thickness of 8.0 $\pm$ 0.5 km is modelled, where crustal thickness

427   is measured from the 6 km s^{-1} isovelocity contour (Fig. 6a). This is ~2 km thicker than standard

428   oceanic crust (White *et al.*, 1992) and is predominantly attributable to the addition of volcanic

429   material in the upper crust. Less than 500 m of crustal thickness may be attributed to underplating or

430   significant thickening of the lower crust.

431

432   **4.3 Pacific plate**

433   Volcaniclastics from Osbourn Seamount cover the Pacific plate to the east end of the seismic profile

434   (Fig. 5d). However, below the volcaniclastics magmatic alteration of the crust is not evident in the

435   seismic velocity structure at offsets greater than 80 km east of the summit where velocities return to

436   those of typical oceanic crust. Pacific plate crust here is modelled from reversed P_n arrivals and has an

437   average oceanic crustal thickness (White *et al.*, 1992) of ~6.5 ± 0.5 km (Fig 6a). Moho geometry is

438   constrained by reversed P_n arrivals between offsets of 20-170 km and upper mantle velocities are low

439   at ~7.6±0.1 km s^{-1}. The travel paths of the P_n diving waves only sample the upper mantle to only ~5

440   km depth beneath the Moho (Fig. 6b). Therefore, the full extent of the low P_n velocity region cannot

441   be constrained from the wide-angle data alone. However, gravity modelling indicates that the low

442   velocity, and hence low density, region beneath the subducting plate may not reach a significant depth,

443   as a reduction in upper mantle density beneath this region is not required to fit the free-air anomaly

444   (Figs 6c and d, offsets 0-150 km).

445   Although only observed over short offset ranges and with long travel-paths in the less-well

446   constrained outer forearc lower crust, P_mP arrivals provide some constraint on the depth and geometry

447   of the subducting plate Moho (Figs 6a and b, offsets -35 to -15 km). Moreover, combined with the

448   low-density of the mantle wedge, this subducted slab geometry extrapolated to depth also produces a

449   good fit to the amplitude and wavelength of the free-air anomaly of the forearc (Fig. 6c).

450

451   **5. DISCUSSION**

452   To characterise the mode of deformation of the subducting and overriding plates when undergoing

453   seamount subduction (Profile A), and the north-to-south migration of this deformation along the

454   forearc, results from previous studies in pre- and post collision zones are used for comparison. Results

455   from SO215 MCS profile D recorded ~150 km to the south (Fig. 2d) (Funnell *et al.*, 2014) highlights

456   the pre-collision zone, Kermadec subduction, structures. Approximately 150 km to the north, a travel-

457   time inversion model produced by Contreras-Reyes et al. (2011) of wide-angle data acquired during a

458   previous R/V Sonne cruise (SO195a) highlights the post-collision zone structures of Tonga

459   subduction (Figs. 1 and 9b, Profile P02).

460

461   **5.2 Pre-collision zone**

Seismic velocity structure of the Tonga-Kermadec - Louisville Ridge collision zone

462   Distinct changes in the shape of the ridge and trench slope occur between the Tonga and Kermadec

463   sections of the subduction zone. In contrast to the flat-topped Tonga Ridge, south of the collision zone

464   the Kermadec Ridge is narrow and the arc and ridge are co-incident. The trench-slope here is ~160

465   km wide with a shallowly dipping upper-trench slope. Although this region is south of the Louisville

466   Ridge collision zone, changes forearc structure over a broad region is evident in the bathymetry data

467   with the ridge broadening from here into the collision zone (Fig. 2). A bathymetric high in the middle

468   of the trench slope is not observed south of Profile D (Fig. 2c) but may be semi-continuous to the

469   north merging with the outer-arc high on Profile A (Funnell *et al.*, 2014). This feature along with the

470   inferred uplift of the Kermadec forearc (Ruellan *et al.*, 2003) may indicate that the structural changes

471   evident between the northern Kermadec Ridge and the southern Tongan Ridge (i.e. from the pre- to

472   current collision zone) are transitional between these two profiles. This transition in ridge structure

473   between the collision and pre-collision zones may be due to pre-existing forearc structures.

474   Alternatively, the deformation may be related to the far field effects of subduction of the thickened

475   crust of the Louisville Ridge at the trench, although the ~150 km distance south of the seamount

476   flexural moats makes this less likely.

477   Tectonic erosion of the overriding plate in the pre-collision zone is inferred as subduction of the

478   Pacific plate at the Tonga-Kermadec Trench is fast (DeMets *et al.*, 1994) and sediment poor (Heuret

479   *et al.*, 2012) with graben on the outer rise having little sediment fill (Profile D, Fig. 2d) (Funnell *et al.*,

480   2014). Moreover, previous multichannel seismic reflection lines in the area image horst and graben

481   structures on the Pacific plate subducted below the outer forearc (von Huene & Scholl, 1991). Formed

482   in response to increased flexure and curvature of the subducting plate at the outer rise, the graben

483   create a rough plate surface which can erode the overriding plate and deform the forearc (Hilde, 1983;

484   Ballance *et al.*, 1989). Tectonic erosion is thus a normal feature of this plate boundary (Clift &

485   MacLeod, 1999) and is evidenced by extensional deformation across the mid- and lower-trench slopes

486   (Fig. 7c). The down-faulting of the east side of the mid-slope terrace, which has left exposed

487   sediments on the footwall (Fig. 7c) (Funnell *et al*., 2014) and extensional collapse of the steep lower-

488   trench slope at the trench (Fig 2d) indicate that the forearc in the pre-collision zone is extending

489   across most of the trench slope and undergoing gravitational collapse (von Huene & Scholl, 1991;

490   Stern, 2011).

491

492   **5.3 Collision zone**

493   On the broad, elevated, and flat-topped Tonga Ridge sediment deposition rates and layer thicknesses

494   vary with time (Herzer & Exon, 1985; Tappin *et al*., 1994) and record the tectonic history of the ridge

495   that proceeded from the initial subduction initiation to uplift associated with the opening of the back-

496   arc. A more recent uplift event in the Quaternary (Tappin *et al.*, 1994) attributed to the subduction of

497   the Louisville Ridge Seamount chain is also inferred (Herzer & Exon, 1985). Although this uplift is

498   inferred to be minor, only ~300 m at most (Clift, 1994). The ridge is currently ~300 m higher than in

499   the post-collision zone to the north and the Kermadec Ridge to the south and it terminates in the east

500   against a steep upper-trench slope. A deformation front at the upper-trench slope—outer-arc high

501   transition is inferred, separating stable ridge from the extending trench slope. However, the outer-arc

502   high also has distributed small-scale extensional faulting (Fig 7d, offset -100 km) and unlike the rest

503   of the ridge on Profile A, the accommodation space produced by this faulting has not yet filled with

504   sediment indicating that the deformation may also be moving arcward.

505   A major change in stress regime on the mid-trench slope is inferred from MCS data acquired

506   across other subduction zones (von Huene & Culotta, 1989). In the collision zone, isovelocity

507   contours in the middle crust step down towards the trench indicating (Fig. 9d) the scale of the present

508   extensional deformation. In addition, block faulting across the mid-trench slope offsets the seafloor

509   with high relief. A ~2 km high block with similar velocities to that of the Eocene arc crust is

510   interpreted as a fragment of the old arc that has slumped into the trench (Fig. 9d offsets -45 to -35 km),

511   with the lower velocities beneath the block indicating extension of the trench slope crust. The high

512   may be elevated due to underplating beneath the trench slope of subducted sediment, seamount

513   derived material or the eroded outer forearc (Fisher *et al.*, 1998; Sak *et al.*, 2009).

514   The Moho beneath the mid- and upper-trench slope overlies mantle wedge where

515   serpentinisation is expected, and where reflectivity from the base of the crust is not observed. The

516   seismically opaque zone is of a similar width (~60 km) to the serpentinised zone in the Cascadian

517   forearc and at most other Pacific Rim subduction zones (Brocher *et al*., 2003; Bostock *et al*., 2002;

518   Hyndman & Peacock, 2003). This is also in-keeping with observations from other Pacific Rim

519   subduction zones where the Moho is either inverted, attenuated or absent due to serpentinisation

520   (Oakley *et al*., 2008; Bostock *et al*., 2002; Stern, 2011; Brocher *et al*., 2003; Cheng *et al*., 2012).

521   Serpentinisation of the mantle wedge is produced by dewatering of subducted sediment and oceanic

522   crust, and may contribute to a blurring of the boundary between crust and mantle (Brocher *et al*.,

523   2003) and a combined reduction in lower crust and upper mantle velocity may occur (Fig 6b). In the

524   proximity of the plate boundary interface blurring of the Moho interface may also be enhanced by

525   basal erosion by rough topography on the subducting plate (Clift & Vannucchi, 2004).

526   Low velocity, fluid-filled trench deposits subducted beneath the forearc can contribute to basal

527   erosion (Clift & Vannucchi, 2004) and in the current collision zone this trench fill is largely supplied

528   by the deforming Osbourn seamount. Small-scale faults imaged by swath mapping of its summit

529   (Lonsdale, 1986) and mass wasting of material from its western flank suggest that the edifice is

530   deforming. As only thin accumulations of sediment are observed on the subducting Pacific plate, the

531   dominant sources of material entering the trench are inferred to be from these faulted flanks.

532   On the eastern side of Osbourn Seamount a semi-continuous reflector in the MCS data,

533   interpreted as the top of the oceanic crust prior to seamount loading, can be traced to 160 km offset

534 where it merges with the reflector of unloaded oceanic crust (Figs 5d and 10). This reflector shows the

535 extent of the seamount moat and a flexural bulge is observed at its seaward termination (Fig. 6a). The

536 distance between the seamount and the crest of the bulge is ~110-120 km and suggests an elastic

537 thickness of ~10 km, consistent with its formation on relatively young oceanic crust at or near a mid-

538 ocean ridge (Watts, 1978).

539   Middle crustal rocks also shoal to the east (Fig. 6a) and suggest the flexural moat formed in

540 response to seamount loading (Watts *et al.*, 1997; Watts & Ribe, 1984), which is also observed at

541 Louisville Seamount further to the east in the chain (Contreras-Reyes *et al.*, 2010). The main

542 difference is that the moat infill dips towards Louisville Seamount but away from Osbourn Seamount.

543 We infer this difference arises because Osbourn Seamount is presently "riding" the Tonga-Kermadec

544 outer rise, which has elevated both the seamount and its flanking moats. The flat summit of the

545 seamount is tilted westward by ~2.5° as it is carried over the outer rise.

546   Upper mantle velocities beneath the outer rise are 8% lower than those observed beneath the

547 seamount chain to the east (Contreras-Reyes *et al.*, 2010). These reduced mantle velocities are

548 indicative of either serpentinisation (Contreras-Reyes *et al.*, 2011; Hyndman & Peacock, 2003) or

549 anisotropy (Savage, 1999) and are modelled here to at least 150 km seaward of the trench. The broad

550 zone over which the reduced mantle velocities are observed may indicate the extent over which

551 bending related stresses act on the oceanic lithosphere as it passes over the outer rise.

552

5.4 Post-collision zone

554 Seamount subduction is inferred to have occurred in the post-collision zone at ~0.5 to 1 Ma (Ruellan

555 *et al.*, 2003). The ridge here is ~100 m deeper and trench-perpendicular canyons transport sediment

556 from the Tonga Ridge towards the trench (Fig. 7a). These canyons feed sediment into two small, ~1-

557 km-deep, sediment-filled basins formed oblique to the trench on the mid-trench slope (Fig. 9a, offsets

558 -50 and -70 km). A region of ~0.3 km s^{-1} lower velocities (Fig. 7a - offsets of -40 and -70 km),

559 compared to the Tonga Ridge basement, extends to ~7 km depth in the crust indicating distributed

560 deformation of the mid-trench slope. Compared to the collision zone, there is an observed decrease in

561 trench slope relief, and increase in trench slope angle, although block faulting structures and seafloor

562 relief still exceed 1 km (Fig. 9a and c). In contrast to the collision zone, the lower-trench slope is a

563 smooth, steep transition from the basins of the mid-slope down to the trench axis.

564   Seismic velocities in the near surface of the trench are ~1 km s^{-1} faster in the post-collision zone

565 and are thus, less likely to be due to seamount derived material. The trench is devoid of significant

566 relief (Fig. 9a), and is comprised of a 6-km-thick zone of relatively low velocity (~5.5 km s^{-1}) above

567 the plate boundary (Figs 8 and 9b). A large part of the forearc crust here is interpreted to be of this

568 low velocity material (Contreras-Reyes et al., 2011). A lower crust of velocity 6-7 km s^{-1} comprises

569 the remaining 5 km, resulting in a total crustal thickness of only ~9 km in the plate boundary zone and

Seismic velocity structure of the Tonga-Kermadec - Louisville Ridge collision zone

570 a down-dip plate interface width of ~21 km (Fig. 9b) (Contreras-Reyes *et al.*, 2011), a 3 km decrease

571 in crustal thickness and 5 km decrease in plate boundary interface width compared to the collision

572 zone. These structures and the reduction in crustal and plate interface width in the post-collision zone

573 are indicative of a greater degree of extensional collapse of the trench slope and its increases in

574 steepness indicates that the forearc may be eroding back to its pre-collision geometry (Lallemand *et*

575 *al.*, 1992).

576   As in the pre-collision zone to the south, away from the influence of the seamount chain, the

577 subducting Pacific plate has generally trench-parallel normal faults on the seaward wall of the trench

578 with vertical offsets as high as 1.5 km with horst and graben widths up to 10 km (Fig. 2d). A zone of

579 relatively low upper crustal velocities of (V_p=4.0-5.5 km s^{-1}) extends to ~3 km beneath the seafloor

580 (Fig. 9b, offsets -30-0 km). Moreover, lower velocities are interpreted in the mid-crust beneath outer

581 rise graben (Fig. 9b, V_p of 6.0-6.2 km s^{-1}, offsets 10–20 km) and in the mantle wedge (Fig. 9b, V_p of

582 7.3-7.5 km s^{-1}) and are inferred to result from pervasive faulting and serpentinisation from deep

583 penetrating fluids (Contreras-Reyes et al., 2011). In the collision zone, alteration of the crust due to

584 Louisville Ridge magmagenesis likely masks the full extent of extensional deformation of the oceanic

585 crust as it passes over the outer rise. In the post-collision zone, however, the extent of the deformation

586 is evident in reduced velocities from the seafloor to the upper mantle (Contreras-Reyes et al., 2011).

587

588 **5.5 Southward migrating seamount subduction**

589 Migration of depocentres from north-to-south along the forearc has been attributed to the sequential

590 uplift of the Tonga Ridge north of the study area, in response to the southward progressing Louisville

591 Ridge subduction (Austin *et al.*, 1989). Previous studies have concluded that seamount subduction is

592 recorded as an angular unconformities within the sediment of perched basins located on the forearc

593 (Clift *et al.*, 1998). A progressive trenchward increase in dip of forearc sediment with depth beneath

594 seafloor is measured at ODP site 841 at 23.3°S (Fig. 1) and interpreted to reflect basal erosion and

595 progressive rotation of the forearc towards the trench. At this site, an increase in rotation rate at 0.5

596 Ma is attributed to collapse of the forearc in the wake of subduction of the Louisville Ridge (Clift &

597 MacLeod, 1999; MacLeod, 1994). However, a period of arcward rotation of sediments during

598 seamount collision with the trench is also inferred from changes in dip angle between pre- and post-

599 collision sediment (Clift *et al*., 1998; MacLeod, 1994). In the context of the above interpretation, we

600 suggest that the arcward-tilted sediment in the mid-slope basin on Profile A records the onset of

601 seamount subduction at the trench in the current collision zone. As the sediment is tilted arcward at a

602 small angle and is not overlain by flat-lying deposits, this rotation is most likely a recent event.

603   Around 135 km of forearc erosion is inferred to have occurred at the Tonga Trench since the

604 Eocene, of which, ~80 km is attributed to subduction of the Louisville Ridge (Clift & MacLeod,

605 1999). Thus, erosion due to seamount subduction is likely a significant contributor to the ~80 km

606   lateral offset in the trench at ~23.5°S (Figs 1 and 10). Just to the north of this offset in trench is

607   Horizon Deep, the deepest part of the Tonga Trench, where seafloor depths exceed 10.5 km (Fig. 1).

608   Exposure of the surface of the subducting slab at the great depths of the trench here has been

609   attributed to an increase in slab dip compared to the north (Lonsdale, 1986; Billington, 1980), and the

610   westward retreat of the forearc (Wright *et al.*, 2000) due to erosion in the wake of seamount

611   subduction around 2-3 Ma (Ruellan *et al.*, 2003; Lonsdale, 1986; Pelletier & Dupont, 1990).

612   At ~23°S near Horizon Deep (Fig. 1), the absence of deep canyons is used to infer substantial

613   collapse of the inner-trench slope due to the subduction of the ridge (Wright *et al.*, 2000). This area is

614   yet to re-establish the block faulting and canyon exploiting trench-perpendicular faults that are

615   generally observed along the erosive Tonga-Kermadec margin (Wright *et al.*, 2000), with the slope

616   here having little relief (Figs 1 and 7a). A return to rough relief on the trench slope occurs south of

617   ~24.5°S and is co-incident with an eastward rotation in trench strike, the northern extent of the

618   seismic gap and the approximate extent of the flexural moat of Louisville Seamount (Figs 1 and 10).

619   The change in seismic state of the subduction zone to the south of ~24.5°S may indicate that once

620   seamounts have subducted beneath the forearc Moho, the region returns to a normal slip pattern

621   (Singh *et al.*, 2011; Scholz & Small, 1997). It is unclear whether the change in seismogenesis reflects

622   an unlocking of the plate interface or a reduction in aseismic stress release as the transfer of fluids to

623   the overriding plate wanes or basal erosion of the overlying plate ceases (Singh *et al.*, 2011).

624   Although located only 150 km north of Profile A, the smooth lower-trench slope and decrease

625   in outer forearc crustal thickness and velocity on Profile P02 in the post-collision zone indicate a

626   greater degree of extensional collapse. A reduction in bathymetric relief on the trench slope is

627   observed at other subduction zones where high levels of extensional deformation of the forearc have

628   occurred and is attributed to both gravity driven collapse producing distributed faulting, and the

629   accumulation on the trench slope of mass-wasting debris from higher up the trench slope (von Huene

630   & Ranero, 2003). The trench axis–outer-arc high separation is 10 km less on Profile P02 than on

631   Profile A (Fig. 10), which is in-keeping with observations of apparently missing crust and the retreat

632   of the forearc at erosive margins (Fisher *et al.*, 1998; Lallemand *et al.*, 1992).

633   At the collision zone at ~26°S, the trench shallows by 3 km as it becomes congested with

634   incoming seamount-derived material and Mo'unga Seamount (Fig 7a and 10). Arcward rotation of the

635   inner-trench slope by the impinging seamount is evidenced by the steepness of the plate boundary

636   fault; the small-scale thrust faulting that intersects the seafloor (Fig. 2b inset, offset -10 km) and the

637   rampart of low-velocity material on the up-dip side of the fault (Fig. 2b and inset, offset -5 km).

638   Relief increases on the inner-trench slope, and active deformation of the outer forearc is indicated by

639   large-scale forearc blocks reaching 2 km in relief on the lower-trench slope, and sediment that records

640   arcward rotation of the mid-slope basin.

641   Throughout the collision zone and to the south of the study area, the trench follows an

Seismic velocity structure of the Tonga-Kermadec - Louisville Ridge collision zone

642 approximately constant strike and rapidly regains a ~9 km depth by 100 km south of Osbourn

643 Seamount (Fig. 10). Profile D, ~250 km south of Osbourn Seamount, images a deep, steep-sided

644 trench, and the slab dip increases compared to the collision zone (Bonnardot *et al.*, 2007; Hayes *et al.*,

645 2012). As arc volcanoes are thought to form above a restricted depth range to the subducted slab

646 (England *et al.*, 2004), this increase in slab dip may be linked to the decrease in the arc-trench gap

647 observed (Fig. 10). Although south of the Louisville Ridge collision zone and undergoing "normal"

648 Tonga-Kermadec subduction, faulting and sedimentation patterns on the forearc suggest that this

649 region is also undergoing extensional collapse.

650 Where Louisville Ridge subducts however, a significant departure from this normal Tonga-

651 Kermadec subduction is observed and an area of reduced trench depth and a broad and shallow sloped

652 block-faulted outer forearc, demarks the ~150-km-wide seamount collision zone. However, this

653 departure may be transient and a rapid southward progression of the collision zone and the return to

654 normal Tonga-Kermadec subduction is inferred from the short, ~180 km along-arc transition from

655 pre-seamount to post-seamount subduction forearc structures in as little as 1.5 Ma.

656

657 **6 CONCLUSIONS**

658 A synthesis of the seismic structure and seabed geomorphology along the Tonga-Kermadec

659 subduction zone indicates a north-to-south progression in the degree of forearc deformation. In the

660 current collision zone the key evidence for deformation during seamount subduction include:

661 1. Subduction of Mo'unga Seamount, currently in the centre of the trench, broadens and shallows

662 the trench floor and rotates the plate boundary fault arcward. The plate boundary lies on the west

663 side of this seamount.

664 2. A ~ 5 km thick region of ~ 4 km s^{-1} material fills the trench to the east of Mo'unga Seamount.

665 Mass wasting events off the west side of Osbourn Seamount likely supply a significant amount of

666 the low V_p material to the trench.

667 3. Elevated topographic blocks on the mid-trench slope may represent fragments of the Eocene arc

668 that have slumped into the trench, with the lower velocities at depth reflecting extension of the

669 trench-slope. The blocks may be elevated due to underplating beneath the lower-trench slope of

670 subducted sediment, seamount derived material or the eroded outer forearc.

671 4. The trench slope break is characterised by a ~2 km fault scarp and a seafloor depth increase

672 towards the trench. A ~3 km increase in depth to the middle and lower crustal layers and a

673 decrease in average V_p to 5.9 km s^{-1} occur beneath the mid-trench slope, indicating deformation

674 throughout the crustal column.

675 5. Recent deformation of the forearc is indicated by the arcward tilt of seafloor sediments in the

676 mid-slope basin and the ~300 m elevation increase of the Tonga Ridge in the collision zone,

677 compared to the north and south.

678

Seismic velocity structure of the Tonga-Kermadec - Louisville Ridge collision zone

679   Evidence for the north-to-south changes in forearc deformation due to seamount subduction include:

680

681   1.   Relief on the lower-trench slope is lower in the post-collision zone due to increased erosion in
682   the wake of seamount subduction.

683   2.   The 10 km decrease in trench axis–outer-arc high separation at this location indicates the
684   leading edge of the overriding plate is eroding arcward (west). A ~80 km lateral offset in the
685   Tonga-Kermadec Trench just south of Horizon Deep has been attributed to erosional retreat of
686   the forearc in the wake of seamount subduction.

687   3.   Mid-slope basins in the pre-collision zone are more deformed than those observed to the south.
688   Crustal velocities beneath these forearc basins suggest that extensional deformation extends
689   into the upper crust. In the pre-collision zone in the south, the mid-slope is a broad basin of ~3
690   km stratified sediments with only distributed small scale-extension.

691   4.   The edges of the seismic gap beneath the Tonga forearc roughly coincide with the approximate
692   extent of the Osbourn Seamount flexural moat. Subduction of a seamount and its flexural moat
693   beneath the forearc Moho may control the seismogenesis of the subducting plate, by either
694   releasing the locking stresses, or by removing the source of fluids that may have facilitated
695   aseismic slip on the plate interface.

696

712

Seismic velocity structure of the Tonga-Kermadec - Louisville Ridge collision zone

712   **REFERENCES**

713   Austin, J.A., Taylor, F.W. & Cagle, C.D., 1989. Seismic stratigraphy of the central Tonga
714   Ridge, *Marine and Petroleum Geology,* 6**,** 71-92.
715   Ballance, P.F., Scholl, D.W., Vallier, T.L., Stevenson, A.J., Ryan, H. & Herzer, R.H., 1989.
716   Subduction of a Late Cretaceous seamount of the Louisville Ridge at the Tonga
717   Trench: A model of normal and accelerated tectonic erosion, *Tectonics,* 8**,** 953-
718   962.
719   Becker, J.J., Sandwell, D.T., Smith, W.H.F., Braud, J., Binder, B., Depner, J., Fabre, D., Factor,
720   J., Ingalls, S., Kim, S.-H., Ladner, R., Marks, K., Nelson, S., Pharaoh, A., Trimmer, R.,
721   Von Rosenberg, J., Wallace, G. & Weatherall, P., 2009. Global Bathymetry and
722   Elevation Data at 30 Arc Seconds Resolution: SRTM30_PLUS', *Marine Geodesy,* 32**,**
723   355-371.
724   Billen, M.I., Gurnis, M. & Simons, M., 2003. Multiscale dynamics of the Tonga-Kermadec
725   subduction zone, *Geophys. J. Int.,* 153.
726   Billington, S., 1980. The morphology and tectonics of the subducted lithosphere in the
727   Tonga–Fiji–Kermadec region from seismicity and focal mechanisms solutions,
728   Ph.D., Cornell University.
729   Bloomer, S.H., Ewart, A., Hergt, J.M. & Bryan, W.B., 1994. Geochemistry and origin of
730   igneous rocks from the outer Tonga forearc (site 841). *in Proceedings of the*
731   *ocean drilling program, scientific results*, ed Hawkins, J., Parson, L., Allan, J., et al.,.
732   Ocean drilling program, College Station, Texas.
733   Bonnardot, M.-A., Regnier, M., Ruellan, E., Christova, C. & Tric, E., 2007. Seismicity and
734   state of stress withing the overriding plate of the Tonga-Kermadec subduction
735   zone, *Tectonics,* 26**,** 1-15.
736   Bostock, M.G., Hyndman, R.D., Rondenay, S. & Peacock, S.M., 2002. An inverted
737   continental Moho and serpentinization of the forearc mantle, *Nature,* 417**,** 536-
738   538.
739   Brocher, T., Parsons, T., Tréhu, A., Snelson, C. & Fisher, M., 2003. Seismic evidence for
740   widespread serpentinized forearc upper mantle along the Cascadia margin,
741   *Geology,* 31**,** 267-270.
742   Burns, R.E., Andrews, J.E., van der Lingen, G.J., Churkin, M.J., Galehouse, J.S., Packham, G.,
743   Davies, T.A., Kennett, J.P., Dumitrica, P., Edwards, A.R. & Von Herzen, R.P., 1973.
744   Site 204. *in Initial reports of the Deep Sea Driling Project 21*, ed Texas A & M
745   University, O. D. P. DSDP Deep Sea Drilling Project, Texas.
746   Cheng, W.B., Hsu, S.K. & Chang, C.H., 2012. Tomography of the southern Taiwan
747   subduction zone and possible emplacement of crustal rocks into the forearc
748   mantle, *Global and Planetary Change,* 90-91.
749   Christensen, D. & Lay, T., 1988. Large earthquakes in the Tonga region associated with
750   subduction of the Louisville Ridge, *Journal of Geophysical Research,* 93**,** 13,367-
751   313,389.
752   Christensen, N.I. & Mooney, W.D., 1995. Seismic velocity structure and composition of
753   the continental crust: a global review., *J. Geophys. Res.,* 100**,** 9761-9788.
754   Clift, P.D., 1994. Controls on the sedimentation and subsidence history of an active plate
755   margin. *in Proceedings of the Ocean Drilling Program, Scientific results*, pp. p.
756   173–188.Ocean Drilling Program, College Station,Texas.
757   Clift, P.D. & MacLeod, C.J., 1999. Slow rates of subduction erosion estimated from
758   subsidence and tilting of the Tonga forearc, *Geology,* 27**,** 411-414.

Seismic velocity structure of the Tonga-Kermadec - Louisville Ridge collision zone

Clift, P.D., MacLeod, C.J., Tappin, D.R., Wright, D.J. & Bloomer, S.H., 1998. Tectonic controls on sedimentation and diagenesis in the Tonga Trench and forearc, southwest Pacific, *Geological Society of America Bulletin,* 110**,** 483-496.

Clift, P.D. & Pecher, I., 2003. Tectonic erosion of the Peruvian forearc, Lima Basin, by subduction and Nazca Ridge collision, *Tectonics,* 22.

Clift, P.D. & Vannucchi, P., 2004. Controls on tectonic accretion versus erosion in subduction zones: Implications for the origin and recycling of the continental crust, *Review of Geophysics,* 42**,** 1-31.

Clouard, V. & Bonneville, A., 2005. Ages of seamounts, islands and plateaux on the Pacific Plate. *in Plates, plumes and paradigms*, pp. 71-90, eds Foulger, G. R., Natland, J. H., Presnall, D. & Anderson, D. L. Geological society of America, Special paper.

Contreras-Reyes, E., Grevemeyer, I., Watts, A.B., Flueh, E.R., Peirce, C., Moeller, S. & Papenberg, C., 2011. Deep seismic structure of the Tonga subduction zone: Implications for mantle hydration, tectonic erosion, and arc magmatism, *Journal of Geophysical Research,* 116**,** 1-18.

Contreras-Reyes, E., Grevemeyer, I., Watts, A.B., Planert, L., Flueh, E.R. & Peirce, C., 2010. Crustal intrusion beneath the Louisville hotsopt track, *Earth and Planetary science letters,* 289**,** 323-333.

Crawford, W.C., Hildebrand, J.A., L.M., D., Webb, S.C. & Wiens, D.A., 2003. Tonga Ridge and Lau Basin crustal structure from seismic refraction data, *Journal of Geophysical Research,* 108**,** 6-1, 6-9.

DeMets, C., Gordon, R.G., Argus, D.F. & Stein, S., 1994. Effect of recent revisions to the geomagnetic reversal time scale and estimates of current plate motions, *Geophysical research letters,* 21**,** 2191-2194.

Dupont, J. & Herzer, R., 1985. Effect of subduction of the Louisville Ridge on the structure and morphology of the Tonga arc, *Geology and offshore resources of Pacific island arcs-Tonga region, Earth Science Series.,* 2**,** 323-332.

England, P., Engdahl, R. & Thatcher, W., 2004. Systematic variation in the depths of slabs beneath arc volcanoes, *Geophys. J. Int.,* 156**,** 377-408.

Expedition_330_Scientists, 2012. Expedition 330 summary. *in Proc. IODP, 330: Tokyo (Integrated Ocean Drilling Program Management International, Inc.)*, eds Koppers, A. A. P., Yamazaki, T., Geldmacher, J. & Scientists, E., Tokyo.

Fisher, D.M., Gardner, T.W., Marshall, J.S., Sak, P.B. & M., P., 1998. Effect of subducting sea-floor roughness on fore-arc kinematics, Pacific coast, Costa Rica, *Geology,* 26**,** 467-470.

Fleury, J.-M., Pubellier, M. & de Urreiztieta, M., 2009. Structural expression of forearc crust uplfit due to subducting asperity, *Lithos,* 113**,** 318-330.

Funnell, M.J., Peirce, C., Stratford, W.R., Paulatto, M. & Watts, A.B., 2014. Structure and deformation of the Tonga-Kermadec subduction system in the Louisville Ridge pre-collision zone *Geophyisical Journal International,* 199**,** 1286-1302.

Geist, E.L., Fisher, M.A. & Scholl, D.W., 1993. Large-scale deformation associated with ridge subduction, *Geophysical Journal International,* 115**,** 344-366.

Hayes, G.P., Wald, D.J. & Johnson, R.L., 2012. Slab 1.0: A three-dimensional model of global subduction zone geometries, *Journal of Geophysical Research,* 117**,** 1-15.

Herzer, R. & Exon, N., 1985. Structure and basin anaylsis of the southern Tonga forearc, *Geology and offshore resources of Pacific island arcs-Tonga region, Earth Science Series.,* 2**,** 55-73.

Seismic velocity structure of the Tonga-Kermadec - Louisville Ridge collision zone

Heuret, A., Conrad, C.P., Funiciello, F., Lallemand, S. & Sandri, L., 2012. Relation between subduction megathrust earthquakes, trench sediment thickness and upper plate stress, *Geophysical research letters,* 39**,** 1-6.

Hilde, T.W.C., 1983. Sediment subduction versus accretion around the Pacific, *Tectonophysics,* 99**,** 381-397.

Hyndman, R.D. & Peacock, S.M., 2003. Serpentinization of the forearc mantle, *Earth and Planetary Science Letters,* 212**,** 417-432.

Koppers, A.A.P., Duncan, R.A. & Steinberger, B., 2004. Implications of a non linear 40Ar/39Ar age progression along the Louisville seamount trail for models of fixed and moving hot spots, *Geochemistry Geophysics Geosystems,* 5**,** Q06L02.

Koppers, A.A.P., Yamazaki, T., Geldmacher, J., Gee, J.S., Pressling, N., Hoshi, H., Anderson, L., Beier, C., Buchs, D.M., Chen, L.-H., Cohen, B.E., Deschamps, F., Dorais, M.J., Ebuna, D., Ehmann, S., Fitton, J.G., Fulton, P.M., Ganbat, E., Hamelin, C., Hanyu, T., Kalnins, L., Kell, J., Machida, A., Mahoney, J.J., Moriya, K., Nichols, A.R.L., Rausch, S., Sano, S.-i., Sylvan, J.B. & Williams, R., 2012. Limited latitudinal mantle plume motion for the Louisville hotspot, *Nature Geoscience,* 5**,** 911-917.

Lallemand, S.E., Malavieille, J. & Calassou, S., 1992. Effects of oceanic ridge subduction on accretionary wedges: Experimental modeling and marine observations, *Tectonics,* 11**,** 1301–1313.

Laursen, J., Scholl, D.W. & von Huene, R., 2002. Neotectonic deformatiom of the central Chile margin: Deepwater forearc basin formation in response to hot spot ridge and seamount subduction, *Tectonics,* 21**,** 2-1, 2-27.

Lonsdale, P., 1986. A Multibeam Reconnaissance of the Tonga Trench Axis and its Intersection With the Louisville Guyot Chain, *Marine Geophysical Researches,* 8**,** 295-327.

MacLeod, C.J., 1994. Structure of the Outer Tonga Forearc at Site 841. *in Proc. ODP, Sci. Results*, pp. 313-329, ed J. Hawkins, P., L., Allan, J. et al. (eds.) Ocean Drilling Program, , College Station, Texas.

Malahoff, A., Feden, R.H. & Dleming, H.S., 1982. Magnetic anomalies and tectonic fabric of marginal basins north of New Zealand, *Journal of Geophysical Research,* 87**,** 4109-4125.

Menard, H.W., Natland, J.H., Jordan, T.H. & Orcutt, J.A., 1987. Site 596: Hydraulic piston coring in an area of low surface productivity in the southwest Pacific. *in Initial Rreport*, ed Party, L. S. S. DSDP 91.

Minshull, T.A., Sinha, M.C. & Peirce, C., 2004. Multi-disciplinary, sub-seabed geophysical imaging - A new pool of 28 seafloor instruments in use by the United Kingdom Ocean Bottom Instrument Consortium, *Sea Technology,* 46**,** 27-31.

Moos, D. & Zoback, M.D., 1983. In situ studies of velocity in fractured crystalline rocks, *J. Geophys. Res.,* 88**,** 2345–2358.

Oakley, A.J., Taylor, B. & Moore, G.F., 2008. Pacific Plate subduction beneath the central Mariana and Izu-Bonin forearcs: New insights from an old margin, *Geochemistry Geophysics Geosystems,* 9.

Parson, L.M. & Hawkins, J., 1994. Two-stage ridge propagation and the geological history of the Lau backarc basin, *Proc. Ocean Drill. Program. Sci. Results,* 135**,** 819-828.

Peirce, C. & Watts, A., 2011. R/V Sonne SO215 - Cruise Report, The Louisville Ridge - Tonga Trench collision: Implications for subduction zone dynamics. Department of Earth Sciences, Durham University, Durham.

Seismic velocity structure of the Tonga-Kermadec - Louisville Ridge collision zone

855   Pelletier, B. & Dupont, J., 1990. Erosion, accretion, backarc extension and slab length
856   along the Kermadec subduction zone, Southwest Pacific, *Comptes Rendu de*
857   *l'Academie des Sciences* Paris Ser II, 1657-1664.

858   Pointoise, B., Pelletier, B., Auboin, J., Baudry, N., Blanchet, R., Butscher, J., Chotin, P.,
859   Diament, M., Dupont, J., Eissen, J.P., Ferriere, J., Herzer, R., Lapouille, A., Louat, R.,
860   d'Ozouville, L., Soakai, S. & Stevenson, A., 1986. La Subduction del la ridge de
861   Louisville le long de la tosse des Tonga: Premiers resultats de la campagne
862   SEAPSO (Leg V), *C.R. Seances Acad. Sci. Ser. II,* 11, 911-918.

863   Ruellan, E., Delteil, J., Wright, I. & Matsumoto, T., 2003. From rifting to active spreading
864   in the Lau Basin - Harvre Trough backarc system (SW Pacific):
865   Locking/unlocking induced by seamount chain subduction, *Geochemistry*
866   *Geophysics Geosystems,* 4, 10.1029.

867   Ruellan, E., Lafoy, Y., Auzende, J.-M., Foucher, J.-P. & Dupont, J., 1994. Oblique spreading
868   in the southern part of the Lau Back-Arc Basin (SW Pacific). *in Geology and*
869   *Submarine Resources of the Tonga-Lau-Fiji Region: SOPAC Technical Bulletin*, pp.
870   319-327, eds Stevenson, A. J., Herzer, R. H. & Ballance, P. F.

871   Sak, P.B., Fisher, D.M., Gardner, T.W., Marshall, J.S. & LaFemina, P.C., 2009. Rough crust
872   subduction, forearc kinematics, and Quaternary uplift rates, Costa Rican segment
873   of the Middle American Trench, *Geological Society of America Bulletin,* 121, 992-
874   1012.

875   Savage, M.K., 1999. Seismic anisotropy and mantle deformation: what have we learned
876   from shear wave splitting studies., *Reviews of Geophysics,* 37, 65-106.

877   Scholz, C.H. & Small, C., 1997. The effect of seamount subduction on seismic coupling,
878   *Geology,* 25, 487-490.

879   Singh, S.C., Hananto, N., Mukti, M., Robinson, D.P., Das, S., Chauhan, A., Carton, H.,
880   Gratacos, B., Midnet, S., Y., D. & Harjono, H., 2011. Aseismic zone and earthquake
881   segmentation associated with a deep subducted seamount in Sumartra, *Nature*
882   *Geoscience Letters,* 1119, 308-311.

883   Stern, C.R., 2011. Subduction erosion: Rates, mechanisms, and its role in arc magmatism
884   and the evolution of the continental crust and mantle., *Gondwana Research,* 20,
885   284-308.

886   Sutherland, R., 1999. Basement geology and the tectonic development of the greater
887   New Zealand region: an interpretation from regional magnetic data,
888   *Tectonophysics,* 308, 341-362.

889   Tappin, D.R., 1994. *The Tonga frontal arc basin,* edn, Vol., pp. 157–176, Elsevier,
890   Amsterdam.

891   Tappin, D.R., Herzer, R.H. & Stevenson, A.J., 1994. Structure and history of an oceanic
892   forearc - The Tonga Ridge - 22° To 26° South. *in Geology and Submarine Resources*
893   *of the Tonga-Lau-Fiji Region: SOPAC Technical Bulletin*, pp. 81-100, eds Stevenson,
894   A. J., Herzer, R. H. & Ballance, P. F.

895   Taylor, F.W., Mann, P., Bevis, M.G., Edwards, R.L., Cheng, H., Cutler, K.B., Gray, S.C., Burr,
896   G.S., Beck, J.W., Phillips, D.A., Cabioch, G. & Recy, J., 2005. Rapid forearc uplift and
897   subsidence caused by impinging bathymetric features: Examples from the New
898   Hebrides and Solomon arcs, *Tectonics,* 24, TC6005.

899   Trehu, A.M., Blakey, R.J. & Williams, M.C., 2012. Subducted seamounts and recent
900   earthquakes beneath the central Cascadia forearc, *Geology,* 40, 103-106.

901   von Huene, R. & Culotta, R., 1989. Tectonic erosion at the front of the Japan Trench
902   convergent margin, *Tectonophysics,* 160, 75-90.

Seismic velocity structure of the Tonga-Kermadec - Louisville Ridge collision zone

903   von Huene, R. & Ranero, C.R., 2003. Subduction erosion and basal friction along the
904   sediment-starved convergent margin off Antofagasta, Chile, *Journal of*
905   *Geophysical Research,* 108**,** doi: 10.1029/2001JB001569.

906   von Huene, R. & Scholl, D.W., 1991. Observations at convergent margins concerning
907   sediment subduction, subduction erosion, and the growth of continental crust,
908   *Rev. Geophys.,* 29**,** 279–316.

909   Wang, K. & Bilek, S.L., 2014. Invited review paper: Fault creep caused by subduction of
910   rough seafloor relief, *Tectonophysics,* 610**,** 1-24.

911   Watts, A.B., 1978. An Analysis of Isostasy in the World's Oceans 1. Hawaiian-Emperor
912   Seamount Chain, *Journal of Geophysical Research,* 83**,** 5989-6004.

913   Watts, A.B., Peirce, C., Collier, J., Dalwood, R., Canales, J.P. & T.J., H., 1997. A seismic study
914   of lithospheric flexure in the vicinity of Tenerife, Canary Islands., *Earth and*
915   *Planetary Science Letters,* 146**,** 431-447.

916   Watts, A.B. & Ribe, N.M., 1984. On geoid heights and flexure of the lithosphere at
917   seamounts, *J. Geophys. Res.,* 89**,** 11,152-111,170.

918   Watts, A.B. & Talwani, M., 1974. Gravity anomalies seaward of deep sea trenches and
919   their tectonic implications, *Geophys. J. R. astroc. Soc.,* 36**,** 57-90.

920   Watts, A.B., Weissel, J.K., Duncan, R.A. & Larson, R.I., 1988. Origin of the Louisville Ridge
921   and is relationship to the Eltanian fracture zone system, *Journal of Geophysical*
922   *Research,* 93**,** 3051-3077.

923   Weissel, J.K., 1979. Evolution of the Lau Basin by the Growth of Small Plates. *in Island*
924   *Arcs Deep-Sea Trenches and Back-Arc Basins*, pp. 429-436, eds Talwani, M. &
925   Pitman, W. C. American Geophysical Union, Washington, DC.

926   Wessel, P. & Smith, W.H.F., 1991. Free Software helps Map and Display Data, *EOS Trans.*
927   *AGU,* 441**,** 445-446.

928   White, R.S., McKenzie, D. & O'Nions, R.K., 1992. Oceanic crustal thickness from seismic
929   measurements and rare earth element inversions, *J. Geophys. Res.,* 97**,** 19,683–
930   619,715.

931   Wright, D.J., Bloomer, S.H., MacLeod, C.J., Taylor, B. & Goodlife, A.M., 2000. Bathymetry of
932   the Tonga Trench and Forearc: a map series, *Marine Geophysical Researches,* 21.

933   Zhou, L. & Kyte, F.T., 1992. Sedimentation history of the South Pacific pelagic clay
934   province over the last 85 million years inferred from the geochemistry of DSDP,
935   *Paleoceanography,* 7**,** 441-465.

936
937

937   **FIGURE CAPTIONS**

938

939   **Figure 1.** Location of the Tonga-Kermadec subduction system in the SW Pacific. (a) Relief in the

940   study area shown by a 150 m x 150 m resampled compilation grid of ship track bathymetry

941   measurements from recent cruises, and the GEBCO global 30 arc-second grid (Becker *et al.*, 2009).

942   The solid and dashed black line marks Osbourn Trough, which intersects the trench at ~25.5°S.

943   Profile A (white with red dots for OBS locations) crosses the current collision zone. Additional

944   constraint is provided by Profile P02 (white with blue dots for OBSs locations - (Contreras-Reyes *et*

945   *al.*, 2011) and MCS Profile D (red line) which cross the post- and pre-collision zones in the north and

946   the south respectively. Black arrows give Australian plate-fixed plate convergence directions and

947   rates (DeMets *et al.*, 1994). White arrow shows Tonga-Kermadec Ridge – Louisville Ridge collision

948   zone migration rate. ODP drill site is shown by a red square and black dots show background

949   seismicity for earthquakes >M_b=5. Red stars are M_b=7.4-7.5 earthquakes in the seismic gap. Dashed

950   circle shows the location of the proposed Motuku Seamount of Ballance *et al.*, (1989). Inset: The

951   generalised features of the SW Pacific – the Tonga-Kermadec Ridge, the trench and backarc, and the

952   Louisville Ridge which intersects the trench at ~26°S. The study area (black outline) includes both

953   pre-, current and post-collision lithosphere of both the subducting and overriding plates. HD is

954   Horizon Deep, the deepest part of Tonga Trench. Red triangles are active arc volcanoes. (b) Sketch

955   showing the main components of the subduction system discussed in the text. OAH is outer-arc high,

956   ITS is the inner-trench slope, UTS is the upper-trench slope, MTT is the mid-trench terrace, MTS is

957   the mid-trench slope, LTS is the lower-trench slope, OTS is the outer-trench slope, and OR is the

958   outer rise.

959

960   **Figure 2.** MCS data acquired along Profiles A and D (Funnell *et al.*, 2014). (a) Bathymetry along

961   Profile A (white line). (b) Corresponding MCS data. Main plot data is unmigrated. Blue dashed lines

962   are the layer interfaces from the final wide-angle model (Fig. 6a) converted to TWTT. Note the good

963   correlation with MCS reflections. Inset shows the plate boundary fault on the west side of Mo'unga

964   Seamount. Dashed box shows the location of the inset. (c) Bathymetry along Profile D (white line).

965   (d) Corresponding MCS data from (Funnell *et al.*, 2014). Note the horst and graben on the outer rise.

966   Inset shows the plate boundary fault and trench axis sediment. Red dashed line on all parts shows the

967   trench axis.

968

969   **Figure 3.** Example forearc record section from OBS A24. See Fig. 1 for location. (a) Data have been

970   band-pass filtered at 2-4-25-40 Hz and deconvolved for display purposes. (b) Comparison of

971   modelled and observed travel-times. Vertical bars are travel-time picks with associated uncertainties

972   and black lines are modelled synthetic arrivals to show the fit to observed arrival times. Picks are

973   overlain on data high-pass filtered above 2 Hz. Main phases are labelled. See section 3.2 for phase

Seismic velocity structure of the Tonga-Kermadec - Louisville Ridge collision zone

974   descriptions. (c) Ray diagram for the section of the model covered in a). Model zero offset coincides

975   with the trench axis and positive offsets are to the east, negative offsets to the west. See text for

976   details.

977

978   **Figure 4.** Example inner-trench slope record section from OBS A19. See Fig. 1 for location and Fig.

979   3 for details.

980

981   **Figure 5.** Example Pacific plate record section from OBS A5. See Fig. 1 for location and Fig. 3 for

982   details for parts b) and c). (d) MCS data from the eastern end of Profile A, traversing the eastern flank

983   of Osbourn Seamount and the Pacific plate. Section location is shown by dashed box on the model in

984   c). Note the strong crustal reflector beneath the east flank of the seamount, interpreted as the top of

985   oceanic crust prior to seamount loading, that has been blanketed with material originating from the

986   eruption of the seamount at ~78 Ma. Ray paths for the crustal reflector from OBS A8 are also shown

987   in (c). Moho reflections are observed at the easternmost end of the profile at ~9 s TWTT. Overlain

988   blue dashed lines are the blue wide-angle model layer interfaces in (c) converted to TWTT.

989

990   **Figure 6.** Modelling for Profile A. (a) Final velocity model. Labelled numbers are P-wave velocities

991   in km s^{-1}. Lighter areas are not constrained by ray coverage. (b) Ray coverage. Light grey lines are P$_g$

992   travel paths, darker grey are P$_n$ and P$_m$P. Inverted triangles represent OBS locations. (c) Free-air

993   gravity anomaly. Blue dots show the observed anomaly. The green line is the anomaly calculated

994   from the crustal density model in d) and the red line is the anomaly calculated from the crustal density

995   model in d) plus the subducted slab and low mantle densities below the forearc. (d) Density model

996   derived from the crustal structure of the final velocity model (Fig. 6a), with densities annotated in kg

997   m^{-3}. Blue lines show the Moho on each plate. Dashed line is depth to which lower P$_n$ velocities are

998   observed.

999

1000   **Figure 7.** Comparison of forearc structures. (a) Seabed relief of the Tonga-Kermadec Trench–

1001   Louisville Ridge collision zone. Note the broad zone of deformation in the lower-trench slope in the

1002   centre of the collision zone, and the smoother lower-trench slopes to the north and south. Coloured

1003   lines are locations of MCS data in b), c) and d). Black dots are background seismicity for earthquakes

1004   >M$_w$=5. Numbered arrows show the plate motion vector. (b) Enlarged section of MCS data for the

1005   mid-slope basin on Profile A. Blue dashed lines are the layer interfaces from the final wide-angle

1006   model (Fig. 6a) converted to TWTT. (c) Enlarged section of MCS data for mid-slope basin on Profile

1007   D (Funnell *et al.*, 2014). (d) Enlarged section of MCS data for Tonga Ridge sediment imaged on

1008   Profile A. Blue lines are the interfaces from the final wide-angle model (Fig. 6a) converted to TWTT.

1009

Seismic velocity structure of the Tonga-Kermadec - Louisville Ridge collision zone

1010   **Figure 8.** One-dimensional velocity profiles through the wide-angle models of Profiles A and P02.

1011   Velocity profiles are plotted with depth below seafloor. Offsets refer to offsets in Figs 9b and d. Black

1012   lines are Profile A, grey lines are Profile P02. Dashed lines show the Moho location. Numbers at the

1013   bottom of each profile are average crustal V_p values for each 1D profile. Note the difference in crustal

1014   velocity between Profiles A and P02 in the 1-4 km depth range on the lower-trench slope.

1015

1016   **Figure 9.** Comparison of wide-angle models. (a) Bathymetry along Profile P02. (b) Profile P02 final

1017   velocity model from the post-collision zone (Contreras-Reyes *et al.*, 2011). Seamount subduction is

1018   inferred to have occurred here ~0.5 to 1 Ma (Ruellan *et al.*, 2003). (c) Bathymetry in the collision

1019   zone, along Profile A. (d) Final velocity model for Profile A. P-wave velocities are annotated in km s^{-}

1020 ^{1}. The location of the trench fault (Fig. 2d, inset) is marked with a black, dashed line. Red dashed lines

1021   on all parts show the trench axis.

1022

1023   **Figure 10.** Summary of along-arc variation in the geomorphic features. Along-arc variation in forearc

1024   structures of the Tonga-Kermadec subduction zone have long been attributed to the subduction of the

1025   Louisville Ridge (Herzer & Exon, 1985). Bathymetric data are plotted along profiles to highlight the

1026   main along-arc structural changes. Note the decrease in arc-trench gap between the Tonga and

1027   Kermadec Ridges. The outer-arc high–trench gap decreases between Profiles P02 and A, indicating

1028   greater erosion of the forearc in the north of the study area. Note the changes in the steepness and

1029   shape of the trench slope along the arc. Yellow arrows on the map show direction of forearc retreat.

1030   Red dashed line is location of the trench.

1031

Seismic velocity structure of the Tonga-Kermadec - Louisville Ridge collision zone

Table 1.

	n	**σ**	**Δt$_{rms}$**	**χ^2**
P$_s$ Forearc	122	0.1	0.127	1.634
P$_g$ Forearc	4942	0.1	0.137	1.877
P$_g$ Trench	1542	0.1	0.161	2.587
P$_g$ Osbourn Seamount	2491	0.1	0.144	2.081
P$_g$ Pacific plate	3039	0.05	0.073	2.117
P$_m$P Pacific plate	853	0.15	0.158	1.177
P$_m$P Australian plate	148	0.15	0.179	1.428
P$_n$ Australian plate	651	0.15	0.107	0.509
P$_n$ Pacific plate	1463	0.15	0.125	0.697
P$_l$P (crustal reflections)	155	0.1	0.138	1.573
Model Total	**15402**	**(0.05-0.15)**	**0.161**	**2.294**

Table 1. Assigned pick uncertainties and calculated model misfits (RMS and χ^2 values): n is number of observations, σ is assigned pick uncertainty, Δt$_{rms}$ is the RMS misfit of the model to the picks, and χ^2 is the normalised chi-squared statistic. Normalised χ^2 represents the fit between modelled and observed travel-times relative to the pick uncertainties. Values less than 1 indicate over-fit of the data, and χ^2 values of 1 represent the best obtainable fit. Note that the χ^2 fit for P$_n$ arrivals is less than one. In this case, this reflects the relatively small number of picks rather than a high model certainty at the base of the crust (Table 1). P$_g$ arrivals were assigned an uncertainty of 50 ms for the Pacific plate, and 100 ms for forearc and trench. As SNR was reduced at longer offsets, deeper travelling phases (P$_m$P and P$_n$) were assigned a higher uncertainty of 150 ms.

Table 2.

	ΔZ (km)	ΔV$_p$ (km s^{-1})
Upper and middle crust	0.5	0.05
Lower crust	1	0.1
Forearc Moho (inner)	1	0.1
Forearc Moho (outer 60 km)	2	0.15
Pacific plate Moho	0.5	0.1

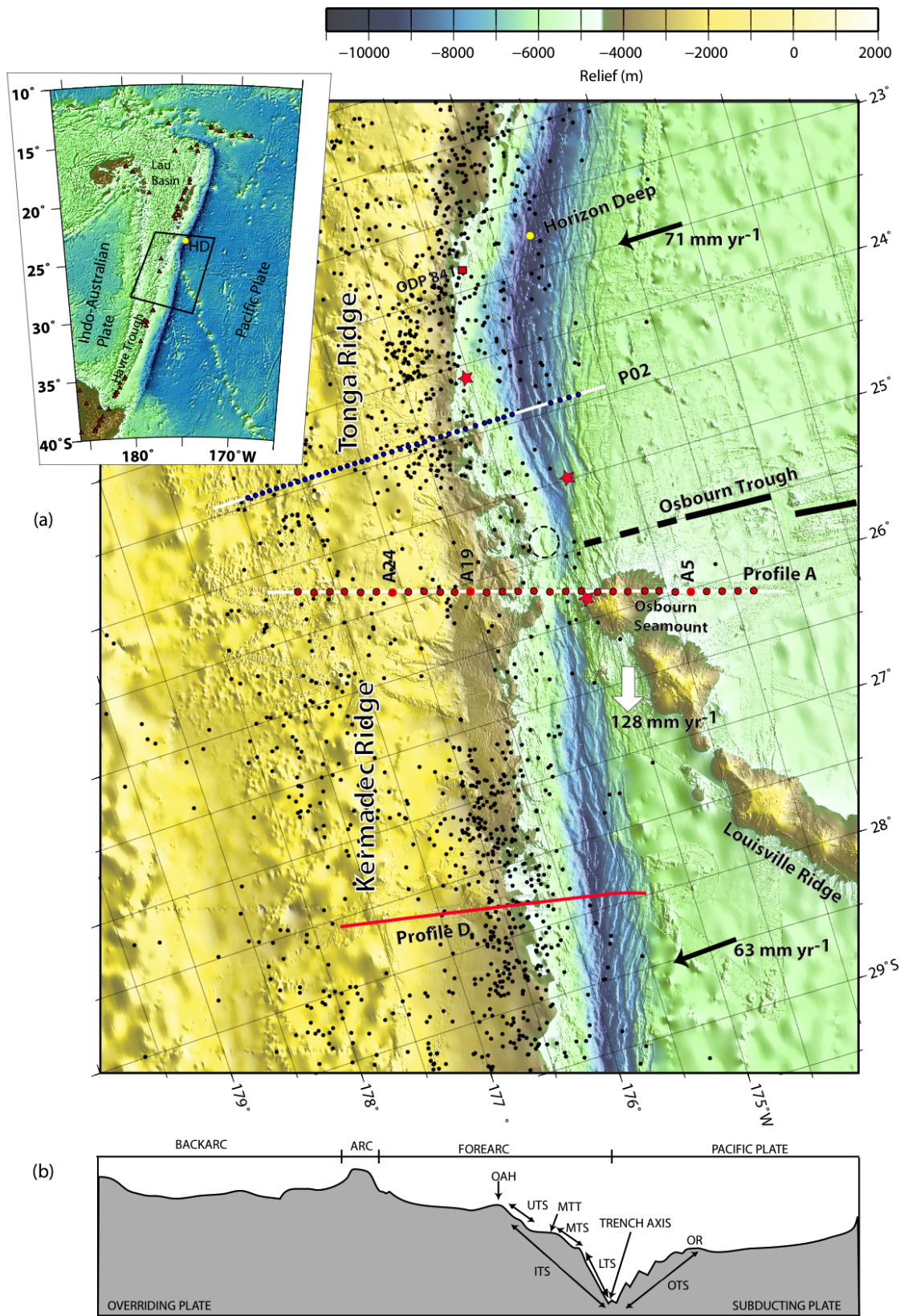**Table 2.** Layer and velocity uncertainties for the wide-angle model.

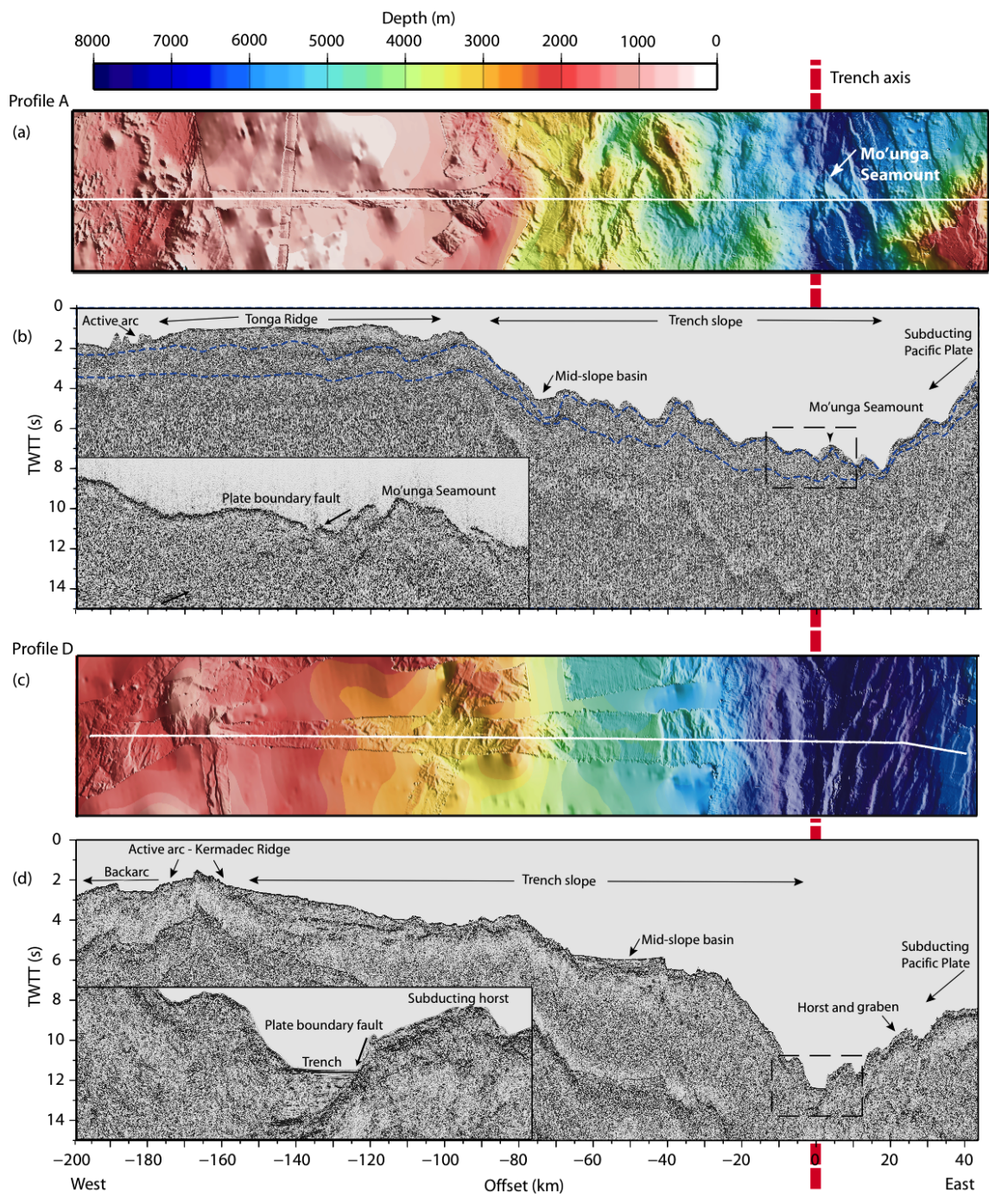*Seismic velocity structure of the Tonga-Kermadec - Louisville Ridge collision zone*

1057   Figure 1.

1058
1059
1060

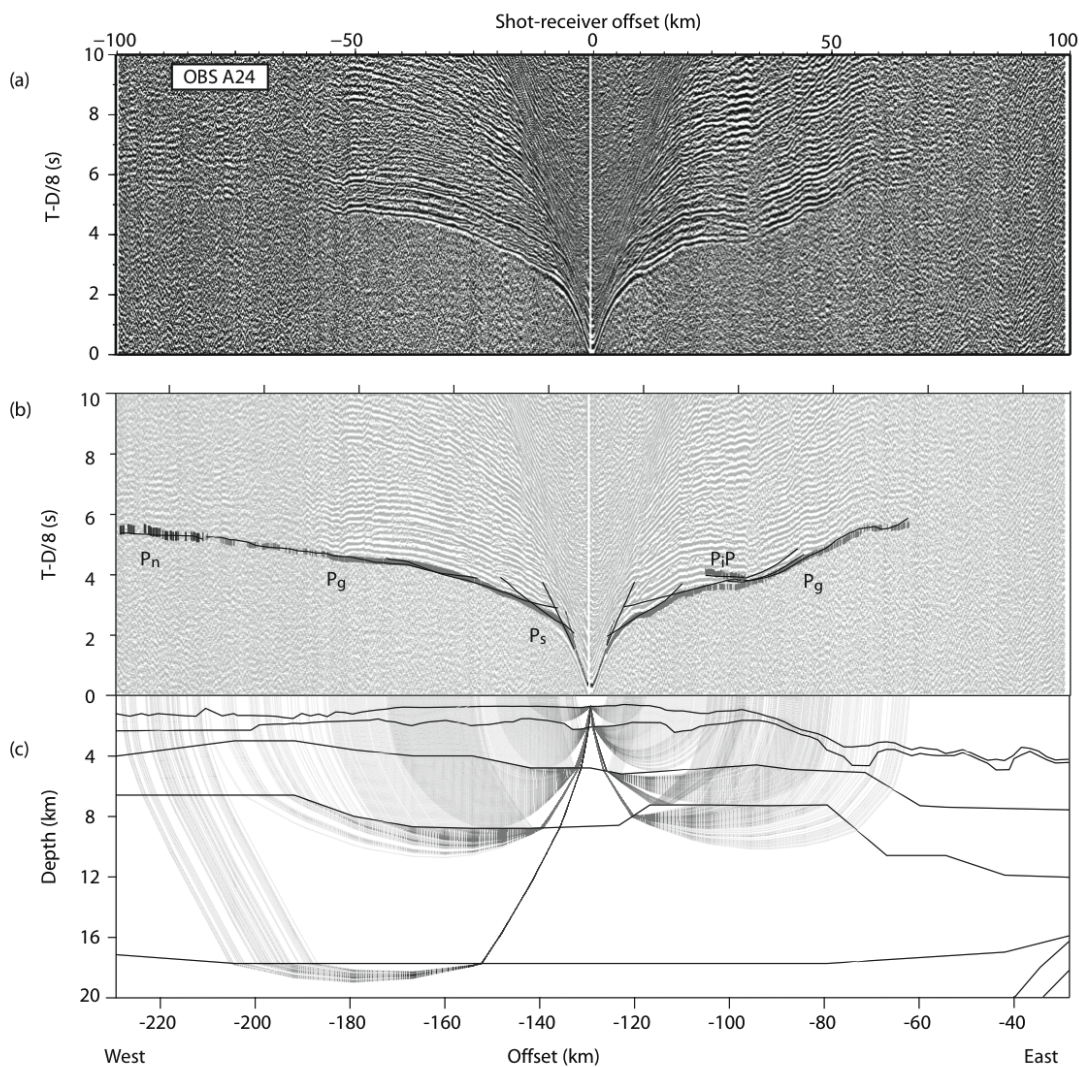*Seismic velocity structure of the Tonga-Kermadec - Louisville Ridge collision zone*

1061   Figure 2.

1062
1063
1064

Seismic velocity structure of the Tonga-Kermadec - Louisville Ridge collision zone
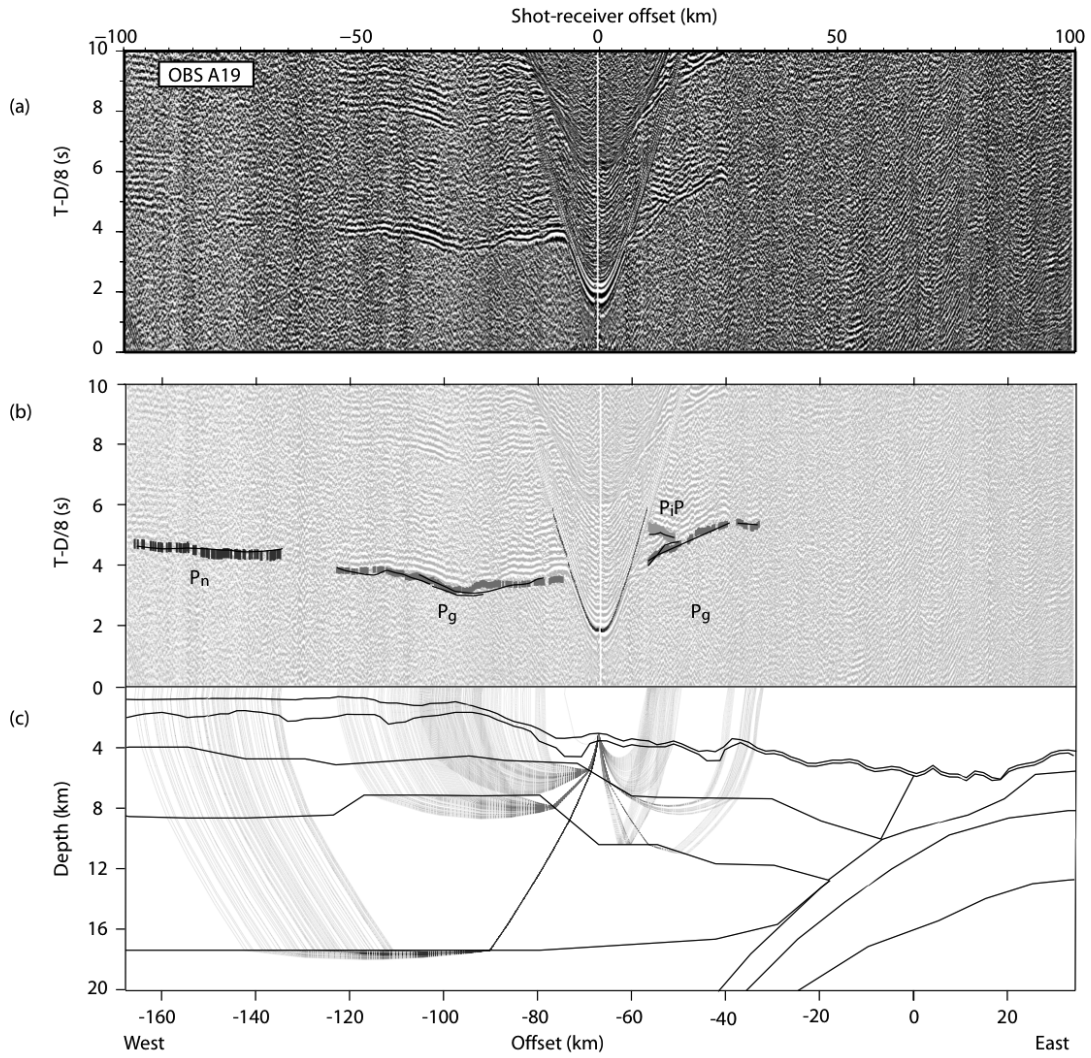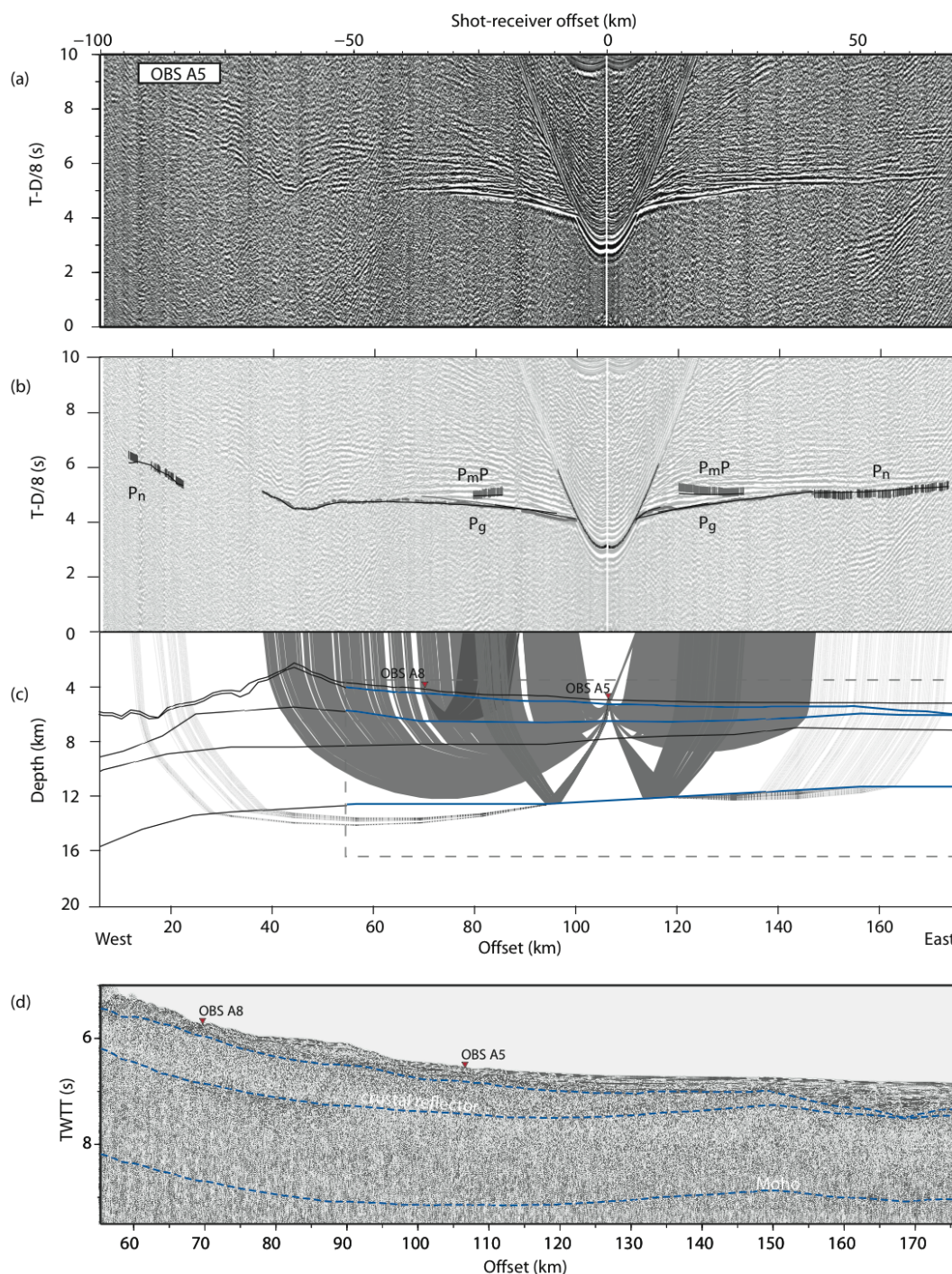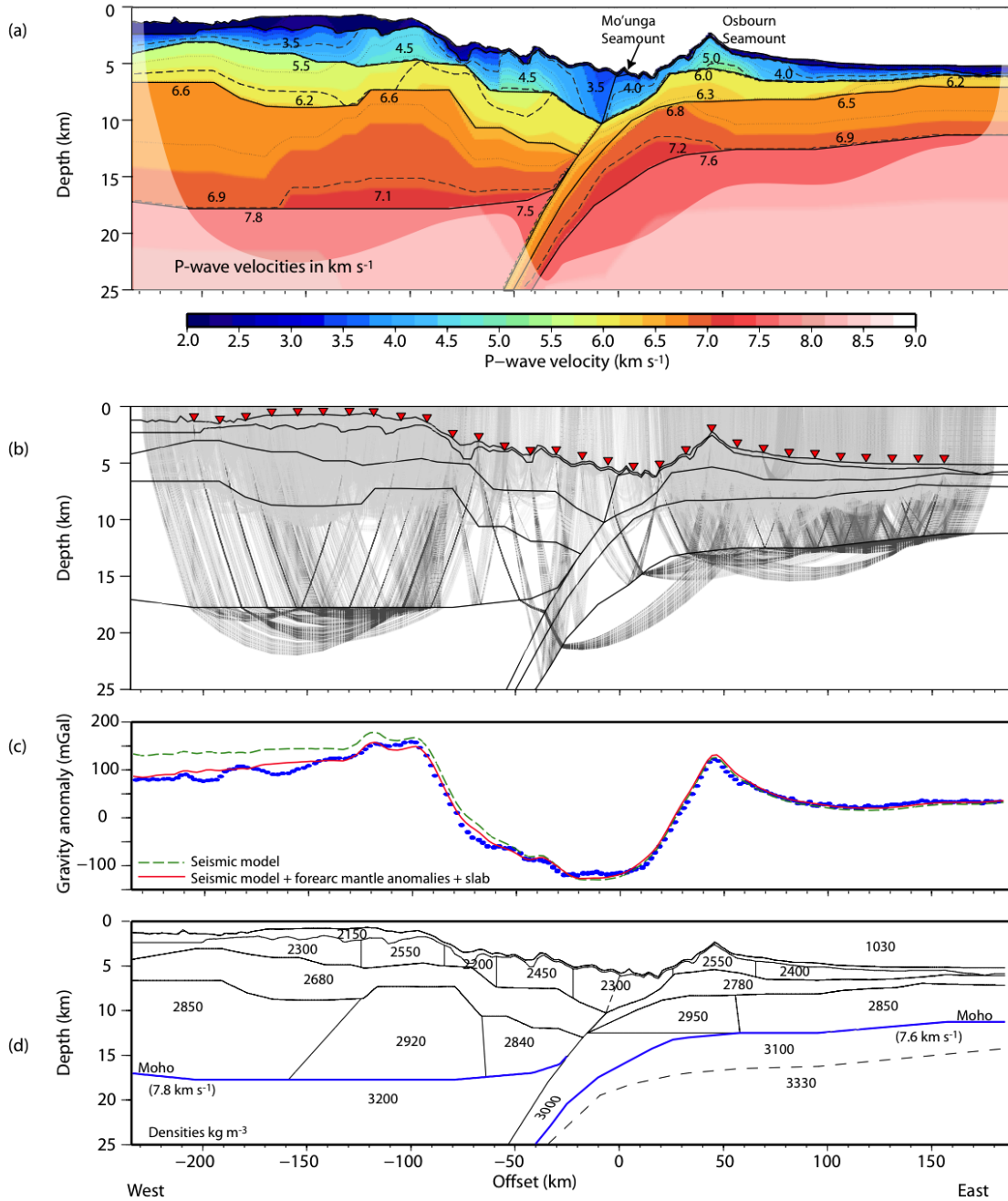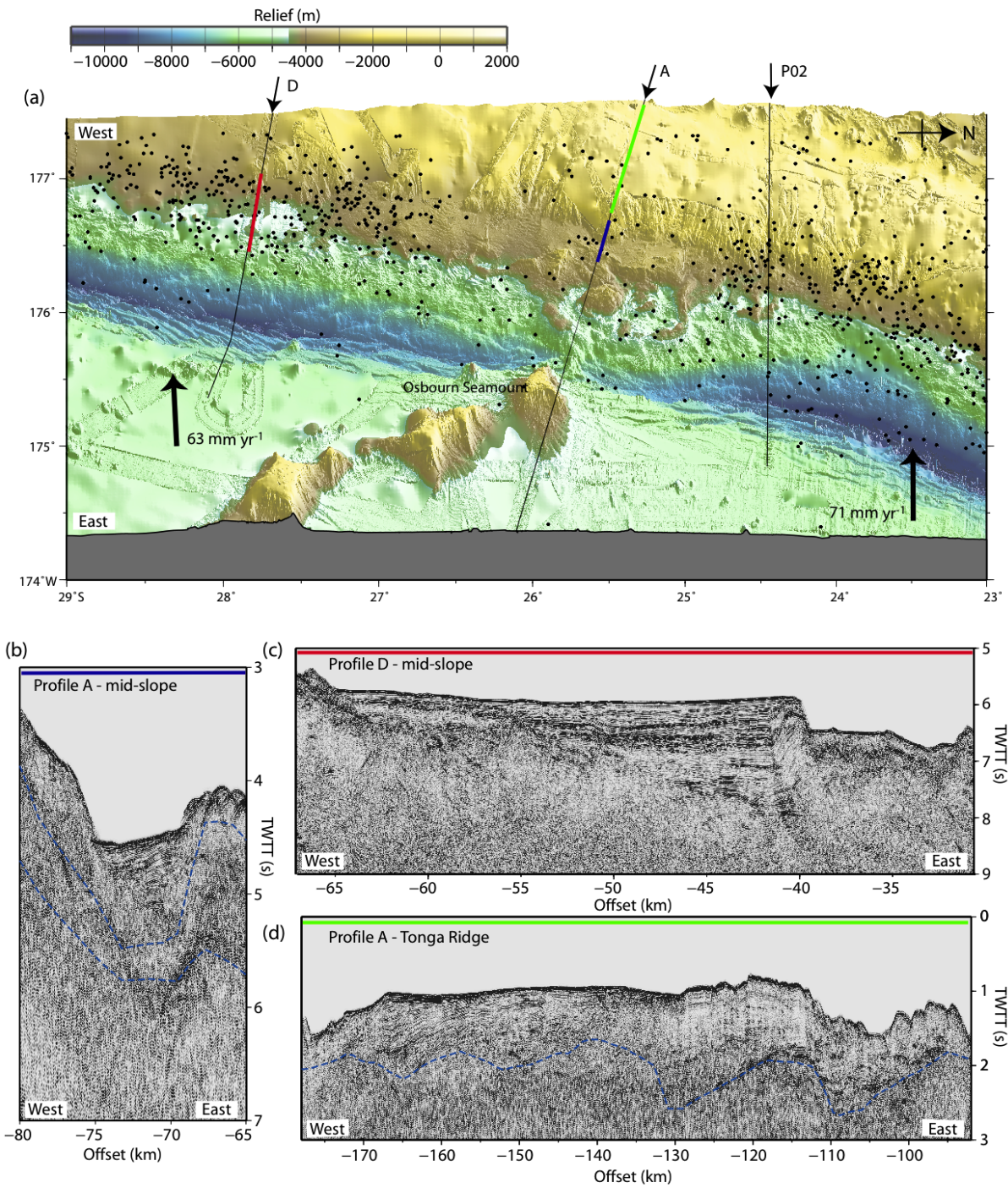
1065   Figure 3.

1066
1067
1068

Seismic velocity structure of the Tonga-Kermadec - Louisville Ridge collision zone
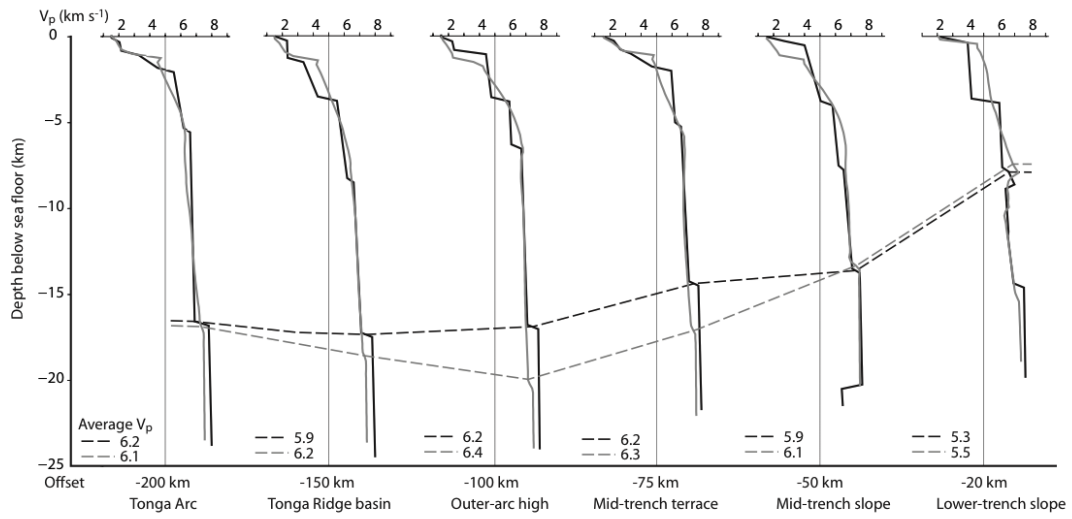
1069   Figure 4.

1070

1071

1072

Seismic velocity structure of the Tonga-Kermadec - Louisville Ridge collision zone

1073　　Figure 5.

1074

1075

1076

Seismic velocity structure of the Tonga-Kermadec - Louisville Ridge collision zone

1077   Figure 6.

1078

1079

1080

Seismic velocity structure of the Tonga-Kermadec - Louisville Ridge collision zone

1081   Figure 7.

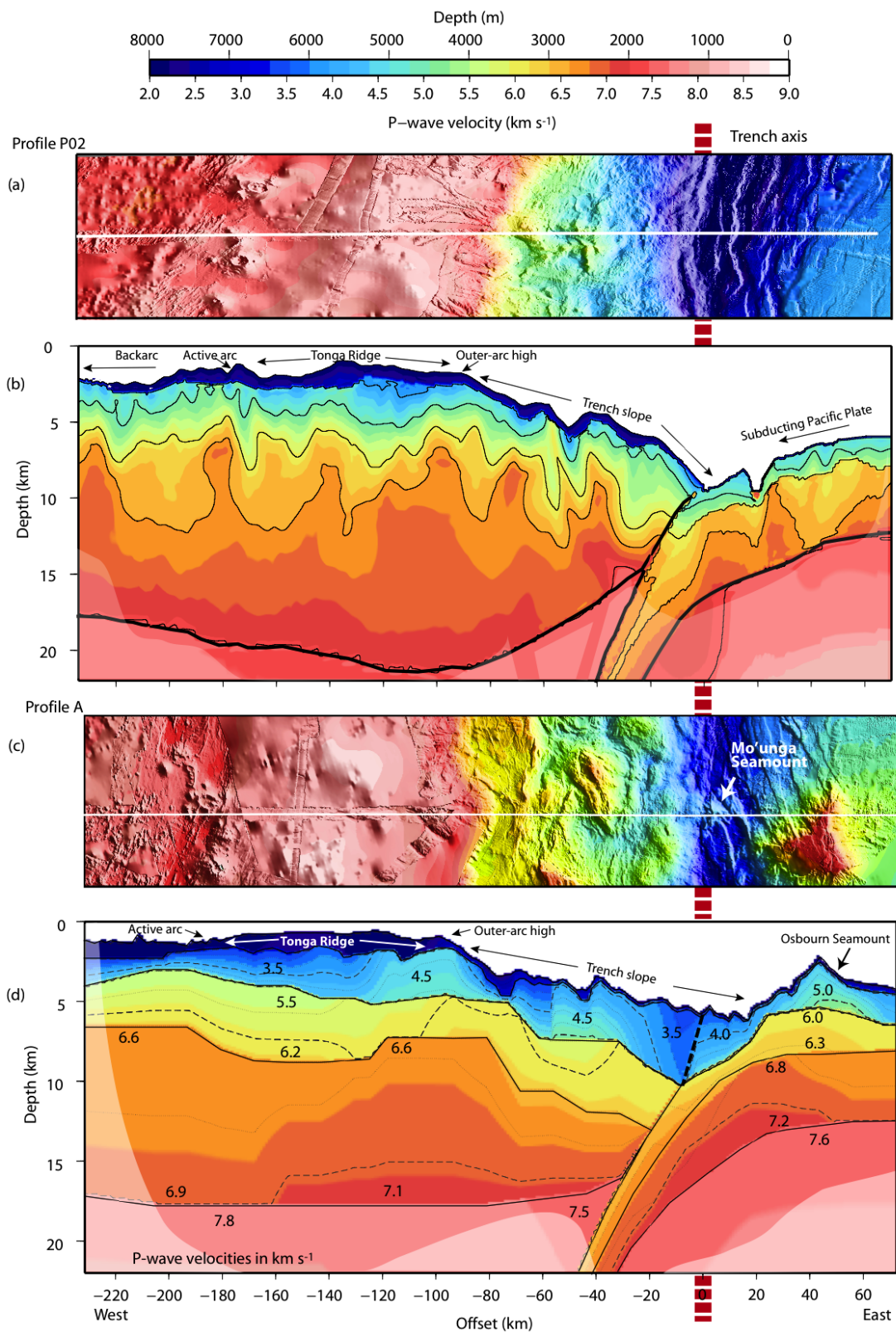1085   Figure 8.

1086

1087

1088

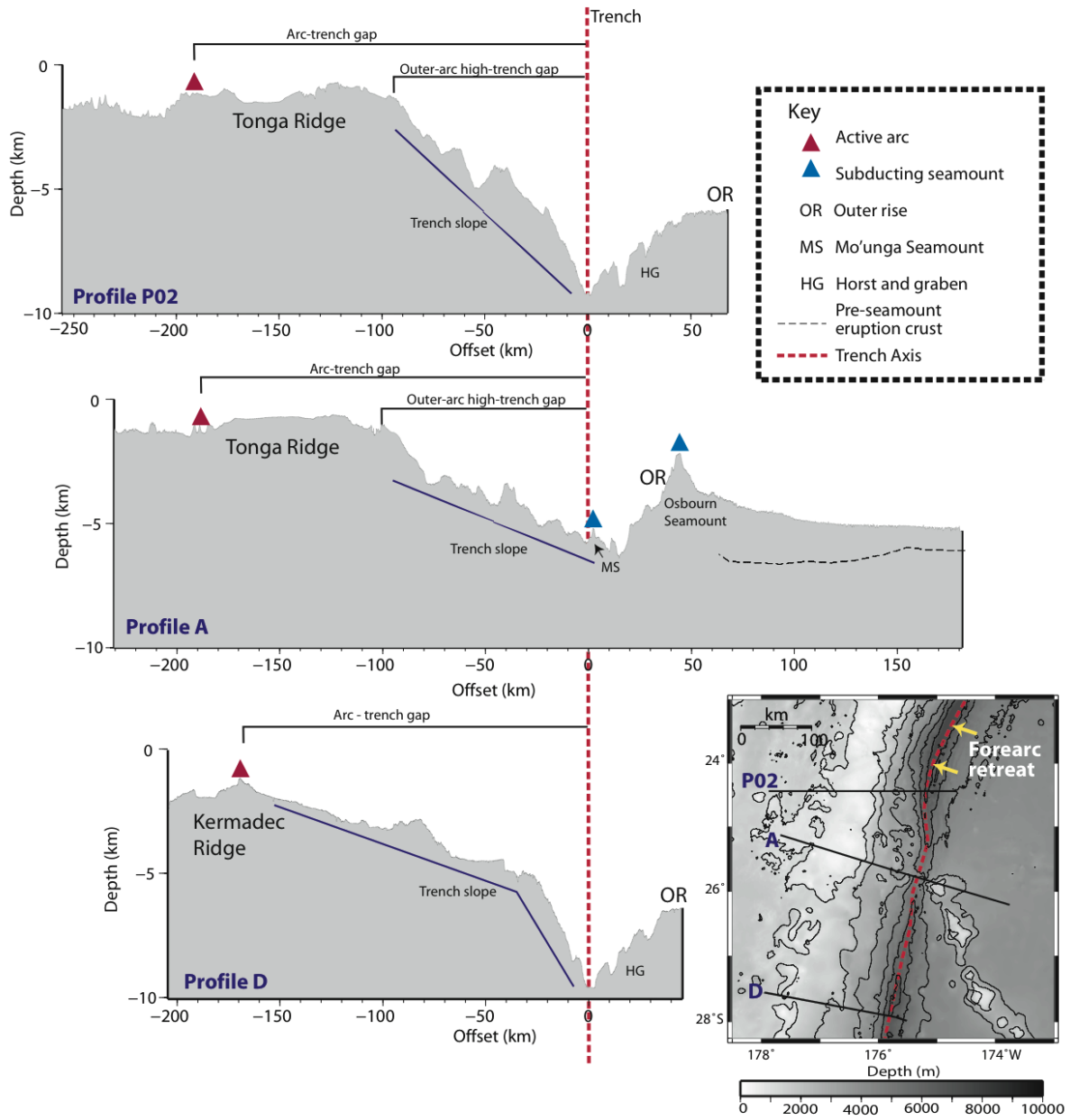*Seismic velocity structure of the Tonga-Kermadec - Louisville Ridge collision zone*

1089   Figure 9.

1090

1091

1092

Seismic velocity structure of the Tonga-Kermadec - Louisville Ridge collision zone

1093   Figure 10.

1094

1095